A!

AALTO UNIVERSITY
School of Electrical Engineering
Department of Radio Science and Engineering

Jan Järveläinen

Operation of a direct-mode bioorganic fuel cell under the influence of an electromagnetic field

Master's thesis submitted in partial fulfillment for the degree of Master of Science in Espoo   .   .2011

Supervisor

Professor Pertti Vainikainen

Instructor

M.Sc. (Tech.) Janne Ilvonen

AALTO UNIVERSITY

SCHOOL OF ELECTRICAL ENGINEERING

ABSTRACT OF THE

MASTER'S THESIS

Author:	Jan Järveläinen
Title of thesis:	Operation of a direct-mode bioorganic fuel cell under the influence of an electromagnetic field

Date:	May 2, 2011	**Number of pages:**	76

Professorship:	Radio engineering	**Code:**	S-26

Supervisor:	Professor Pertti Vainikainen
Instructor:	M.Sc. (Tech.) Janne Ilvonen

In this Master's thesis the influence of a time-harmonic electromagnetic field on the operation of a direct-mode bioorganic fuel cell is investigated. Also coaxial tapering is studied and a tapered matching part is manufactured. The frequency under focus ranged from 50 MHz to 5 GHz.

Today, fuel cells are found very attractive among alternative energy sources due to their clean emissions. Especially bioorganic direct-mode fuel cells, in which the bioorganic fuel and the electrolyte are mixed together, offer an easy-to-use energy source for remote districts. Glucose, for instance, or other sugars could be used as fuel. The main problems related to fuel cells constitute their high cost and the problematic storage and inefficient production of the conventional fuels. Biofuels, on the other hand, are easily stored but yet unable to achieve sufficient power densities. Enhancement of fuel cell efficiency by means of RF energy has been researched earlier with promising results.

This work examines the effect of an electromagnetic field on the output power of a fuel cell, which can be treated electrically as a coaxial cable. The basics of fuel cells, coaxial cable theory and the main characteristics of the fuel cell under study are presented in the first chapters of the thesis. A broadband tapered matching part is designed and constructed in order to enable the feeding of an electromagnetic field inside the fuel cell. Electromagnetic field simulations are exploited in order to optimize the tapering and to gain knowledge of the electromagnetic behavior inside the fuel cell. The main goal is to feed the high-frequency power into the fuel cell under controlled circumstances, since only then can the analysis can be made thoroughly.

The output power measurements of the fuel cell are conducted in order to find a specific or threshold frequency for the EM field, under the influence of which the operation of the fuel cell is enhanced the most. The operation of the fuel cell is measured both with and without coupling an EM signal into the fuel cell and the results are compared. The measurement results obtained so far do not show any indication that the fuel cell operation is enhanced by the RF energy. It is, however, noted that the fuel cell was not operating correctly during the output power measurements, and thus the accuracy of the measurements was decreased. The malfunction was a consequence of a faulty anode catalyst. Hence, further measurements are to be performed in the future with a fully functional fuel cell.

Keywords:	fuel cell, tapering, EM simulations, electromagnetic field, biofuel
Language:	English

Tekijä:	Jan Järveläinen		
Työn nimi:	Suoramoodisen biopolttokennoakun toiminta sähkömagneettisen kentän vaikutuksen alaisena		
Päivämäärä:	2. toukokuuta 2011	**Sivumäärä:**	76
Professuuri:	Radiotekniikka	**Koodi:**	S-26
Työn valvoja:	Professori Pertti Vainikainen		
Työn ohjaaja:	DI Janne Ilvonen		

Tässä diplomityössä tutkitaan aikaharmonisen sähkömagneettisen kentän vaikutusta suoramoodisen biopolttokennoakun toimintaan. Myös koaksiaalista taperointia tutkitaan ja taperoitu sovitusosa valmistetaan. Tarkasteltava taajuusalue ulottui 50 MHz:stä 5 GHz:iin.

Tällä hetkellä polttokennot ovat muiden vaihtoehtoisten energialähteiden joukossa hyvin kiinnostavia päästöjen puhtaudesta johtuen. Erityisesti suoramoodiset biopolttokennot, joissa biopolttoaine ja elektrolyytti sekoitetaan keskenään, tarjoavat helppokäyttöisen energialähteen harvaan asutuille seuduille. Polttoaineena voidaan käyttää esimerkiksi glukoosia tai muita sokereita. Polttekennojen suurimmat ongelmat ovat korkea hinta sekä perinteisten polttoaineiden ongelmallinen varastointi ja tehoton valmistus. Biopolttoaineiden säilytys ei toisaalta vaadi erityistoimenpiteitä, mutta polttoaineet eivät vielä pysty tuottamaan riittävän korkeita tehotiheyksiä. Radiosignaalien tehostavaa vaikutusta polttokennon toimintaan on aikaisemmin tutkittu lupaavin tuloksin.

Tässä työssä yritetään selvittää, onko sähkömagneettisella kentällä vaikutusta sähköisesti koaksiaalikaapelin tavoin käyttäytyvän polttokennon ulostulotehoon. Työn alussa esitetään polttokennon alkeet, koaksiaalikaapelin teoria sekä tutkittavana kohteena olevan polttokennon tärkeimmät ominaisuudet. Laajakaistainen taperoitu sovitusosa suunnitellaan ja valmistetaan jotta polttokennoon voidaan syöttää sähkömagneettinen kenttä. Sähkömagneettista kenttäsimulaattoria hyödynnetään taperoinnin optimoimiseksi ja polttokennon sisäisen sähkömagneettisen kentän käyttäytymisen selvittämiseksi. Päätavoitteena on syöttää korkeataajuinen teho polttokennoon hallituissa olosuhteissa, jolloin analyysi voidaan tehdä perusteellisesti.

Ulostulotehomittausten avulla on tarkoitus löytää tietty taajuus tai kynnystaajuus, jolla sähkömagneettisen kentän vaikutus polttokennon toimintaan on mahdollisimman hyvä. Polttokennon toimintaa tarkastellaan sekä ilman sähkömagneettisen kentän vaikutusta että radiotehon ollessa kytkettynä polttokennoon. Mittaustulokset eivät anna mitään viitteitä polttokennon toimintaa tehostavasta vaikutuksesta. On kuitenkin huomattava, että ulostulotehomittausten aikana polttokenno ei toiminut toivotulla tavalla eikä mittausten luotettavuudesta näin ollen oltu täysin varmoja. Toimintahäiriö johtui viallisesta anodikatalyytista. Mittauksia suoritetaan tulevaisuudessa lisää täydellisesti toimivan polttokennon kanssa.

| **Avainsanat:** | polttokenno, taperointi, sähkömagneettiset simuloinnit, sähkömagneettinen kenttä, biopolttoaine |
| **Kieli:** | Englanti |

Preface

This thesis has been done at the Department of Radio Science and Engineering in collaboration with the Department of Energy Technology at Aalto University.

My supervisor, prof. Pertti Vainikainen, deserves my deepest gratitude for guiding me, not just through the work, but also into a deeper understanding of electromagnetic theory and radio engineering in general. I want to thank him for always having time to answer questions and explain difficult matters thoroughly.

D.Sc. Tommi Laitinen and M.Sc. Janne Ilvonen have instructed me through my work with great expertise and patience. I want to thank Tommi for encouraging me towards critical thinking and deeper investigation also in fundamental questions. Janne deserves thanks for helping me with just about everything and always being available for both insignificant and more important issues.

D.Sc. Jukka-Pekka Spets from the Department of Energy Technology also deserves my gratitude for helping me with the measurements and for introducing me to the world of chemical science. I am also grateful to M.Sc. Jyri Rantanen from Hydrocell, who has been very flexible with developing and manufacturing the fuel cell. (Soon to be) D.Sc. Jari Holopainen deserves special thanks for answering many questions and helping me understanding many matters concerning electromagnetic behavior. I am thankful also to Eino Kahra for helping me with the matching part design and for manufacturing the prototype. Also William Martin deserves thanks for proofreading the final thesis. Many others at the Department of Radio Science and Engineering have also helped me with theoretical pondering and simulator problems. Thank you for keeping up the friendly and educative atmosphere. I would also like to thank my fellow students and friends, "brothers in arms", for long lunches during exhausting days.

My parents, my brother and my sister along with close friends have always encouraged me in my studies, for which I am very thankful. Especially my father has been an exemplary role model for me. Finally, I would like to thank my adorable wife Freja for not asking too many work-related questions at home, and for giving me a wonderful awakening (and breakfast) many mornings. Last, I thank God Almighty, my Creator and heavenly Father, for guiding me to this very interesting field of research.

Espoo, April 8, 2011

Jan Järveläinen

CONTENTS

LIST OF ABBREVIATIONS AND ACRONYMS

AFC	Alkaline fuel cell
atm	Atmospheric pressure
$C_6H_{12}O_6$	Monosaccharide glucose
CoTPP	Pyrolized cobalt porphyrin complex
CTC	Carbon-teflon-catalyst
DC	Direct Current
DMFC	Direct methanol fuel cell
EM	Electromagnetic
FEM	Finite element method
KOH	Potassium hydroxide
MCFC	Molten carbonate fuel cell
$MnCo_2O_4$	Spinel
OCV	Open circuit voltage
Pa	Pascal
PAFC	Phosphoric acid fuel cell
PEMFC	Proton exchange membrane fuel cell
PSU	Polysulfone
QTEM	Quasi Transverse electric magnetic
RF	Radio frequency
SOFC	Solid oxide fuel cell
TEM	Transverse electric magnetic

List of Symbols

Symbol	Meaning
$\vec{B}$	Magnetic flux density [Vs/m^2]
C	Capacitance [F]
C_f	Capacitance of the field inside the sensor [F]
C_l	Capacitance per length [F/m]
C_0	Concentration [mol/dm^3]
C_T	Total capacitance per length [F/m]
c	Speed of light [m/s]
$\vec{D}$	Electric displacement density [As/m^2]
$\vec{E}$	Electric field [V/m]
F	Faraday constant [As/mol]
f	Frequency [Hz]
G	Radiation conductance [S]
$\vec{H}$	Magnetic field [A/m]
h	Planck constant [Js]
I	Current [A]
I_1	Bessel function
IL	Insertion loss [dB]
$\vec{J}$	Current density [A/m^2]
j	Imaginary unit
k	Wave number [1/m]
L	Inductance [H]
L	Length of the taper [m]
L_c	Attenuation [dB]
L_l	Inductance per length [H/m]
l	Length of the operational part of the fuel cell [m]
n	Number of steps in the taper
n_e	Number of transferred electrons
P_{av}	Average power [W]

q	Electric charge [C]
R_s	Surface resistance
r	Radius [m]
r_i	Inner radius [m]
r_o	Outer radius [m]
RL	Return loss [dB]
SWR	Standing wave ratio
T	Temperature [°C]
t	Time [s]
$\vec{u}_r,\ \vec{u}_z,\ \vec{u}_\phi$	Unit vector
V	Voltage [V]
V_{an}	Volume [dm^3]
V_{max}	Maximum voltage[V]
V_{min}	Minimum voltage[V]
V^+	Voltage amplitude of the propagating wave
V^-	Voltage amplitude of the reflected wave
v_p	Propagating velocity [m/s]
W_{heat}	Heat energy [J]
Z	Impedance [Ω]
$Z_0,\ Z_L$	Characteristic impedance [Ω]
α	Attenuation constant
α_c	Conductor attenuation coefficient
α_d	Dielectric attenuation coefficient
β	Wave number [1/m]
Γ	Cross-sectional contour of the conductor
γ	Propagation constant
$\tan\ \delta$	Loss tangent
ε	Permittivity [F/m]
ε_0	Permittivity of vacuum [F/m]
$\varepsilon_d^{''}$	Part of the imaginary part of the permittivity, representing dielectric losses [F/m]
ε_{eff}	Effective relative permittivity
ε_r	Relative permittivity
$\varepsilon_r^{'}$	Real part of the relative permittivity
$\varepsilon_r^{''}$	Imaginary part of the relative permittivity
ε_s	Low-frequency permittivity [F/m]
ε_∞	High-frequency permittivity [F/m]
$\varepsilon^{'}$	Real part of the permittivity [F/m]
$\varepsilon^{''}$	Imaginary part of the permittivity [F/m]

η	Wave impedance [Ω]
λ	Wavelength [m]
λ_0	Wavelength in vacuum [m]
μ	Permeability [H/m]
μ_0	Permeability in vacuum [H/m]
ρ	Electric charge density [As/m^3]
ρ, ρ_0, ρ_L	Voltage reflection coefficient
ρ_m	Maximum passband ripple
σ	Conductivity [S/m]
σ_l	Conductivity per length [S/m]
τ_D	Relaxation time [s]
τ_L	Voltage transmission coefficient
Φ	Electric potential [V]
ϕ	Angle of the reflection coefficient [°]
ω	Angular frequency [rad/s]

CHAPTER 1

INTRODUCTION

During particularly the last decade, renewable energy sources have been gaining great interest. Along with, for example, wind and solar energy, attention has been directed also to fuel cells, especially due to their clean emissions. Particularly remote districts in developing countries would benefit greatly of a user friendly bioorganic fuel cell fueled with, for instance, sugar.

Direct-mode, bioorganic fuel cells are easy-to-use and emit no pollutants, but when using glucose as fuel they have very low current density and power levels, which is a major obstacle for the profitability. The oxidation reactions occur at a level of only one twelfth of the theoretical maximum [1], which gives a reason to believe that the potential efficiency is considerably higher than the present efficiency. Recent research [2,3] on the subject suggests that feeding electromagnetic signals from a signal generator into the fuel cell could enhance the output power levels and thus contribute to the bioorganic fuel cell commercialization process.

The purpose of this work is to investigate the influence of a time-harmonic electromagnetic field on the operation and efficiency of the fuel cell. The frequency range extends from 50 MHz to 5 GHz, which is chosen according to previous research results [4]. The work is performed as a collaboration between the Department of Radio Science and Engineering and the Department of Energy Technology at Aalto University. The former has focused on the implementation of the feed of the electromagnetic field, while the latter has been responsible for the development of the fuel cell and the chemical part of the project. Hydrocell Ltd. has also contributed to the work by manufacturing the fuel cells.

The thesis is organized as follows. First, the basics of fuel cells are introduced concisely in Chapter 2. In Chapter 3, coaxial cable theory is presented, and Chapter 4 covers the configuration and properties of the fuel cell under test along with the material mea-

surements. Chapter 5 examines the implementation of the feed of the time-harmonic electromagnetic field and the matching problem between the signal generator and the fuel cell. Tapering is discussed in particular. In Chapter 6, the measurement practice and results are presented. The last chapter concludes the work and presents future prospects.

CHAPTER 2

FUEL CELL BASICS

Fundamentally, a fuel cell is an alternative energy source, which was invented already in the 17th century [5]. This chapter introduces the basic operating principle of the fuel cell along with the typical classification of different fuel cell types. Also fueling and performance are discussed.

2.1 Introduction

A fuel cell is an electrochemical device that converts chemical energy into electrical energy. The reaction requires a fuel, an oxidant and an electrolyte to produce the electrical energy as well as heat and water [6–8]. Hydrogen is usually used as fuel and air as the oxidant. The elementary chemical reaction occurring in the fuel cell can be written as [6–8]

$$2H_2 + O_2 \leftrightarrow 2H_2O, \tag{2.1}$$

and is the opposite of *electrolysis*, where water is separated into hydrogen and oxygen by electric current [6]. Additionally, a fuel cell consists of two electrodes; the anode (negative electrode) and the cathode (positive electrode). The basic fuel cell configuration is shown in Fig. 2.1. In order to increase the produced current, the electrodes should be flat and the thickness of the electrolyte small. Moreover, the electrodes ought to be porous providing optimal penetration for the electrolyte and the gases [8]. This increases the fuel cell efficiency by giving the maximum area of contact between the electrodes, electrolyte and gases [6, 8]. A closer investigation of the reactions occurring on both electrodes is needed in order to understand the function of the fuel cell. At the anode, the hydrogen atoms (fuel) ionize and release electrons, thus creating protons. Here, energy is released and the equation can be written as [6]

$$2H_2 \rightarrow 4H^+ + 4e^-. \tag{2.2}$$
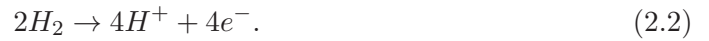
The protons pass through the electrolyte to the cathode and simultaneously the electrons tread a different path through the electrical circuit from the anode to the cathode. The reaction at the cathode combines the oxygen with the electrons and the protons, and concurrently forms water [6]:

$$O_2 + 4e^- + 4H^+ \rightarrow 2H_2O. \tag{2.3}$$
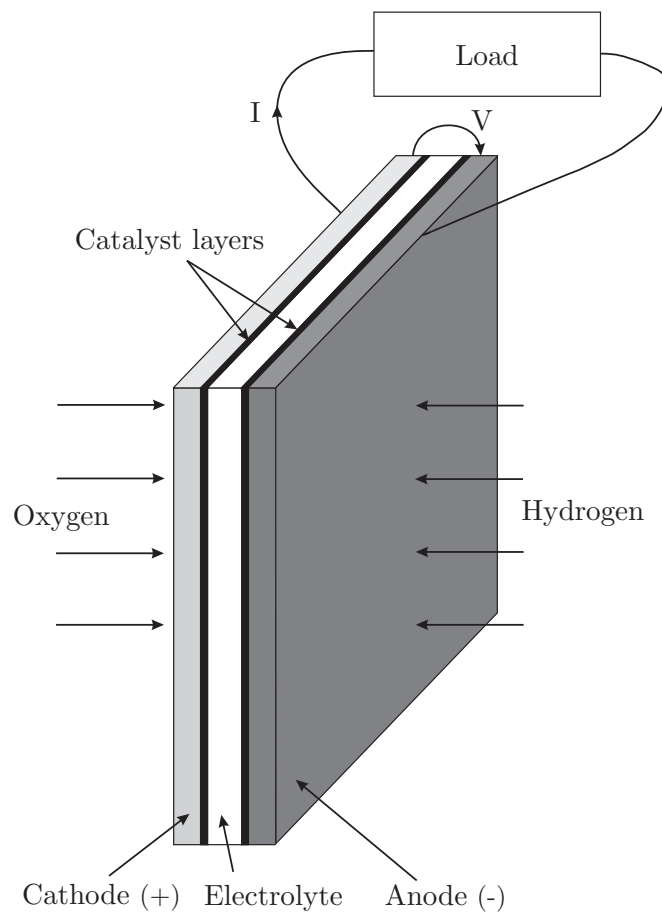
Fig. 2.1: Basic construction of a fuel cell. Hydrogen is extracted from the fuel and oxygen from the air.

The primary advantage of a fuel cell over a battery is that fuel cells do not require recharging [8]. This is due to the fact that batteries are energy *storage* devices, whose energy decreases when the chemical reactants are consumed, whereas fuel cells are energy *conversion* devices and can theoretically produce energy for as long as fuel is supplied to the anode and an oxidant is supplied to the cathode [7, 9]. Other advantages include

silent operation and no emission of pollutants [10].

Gaseous hydrogen is the most common fuel and can be extracted from several sources, for instance natural gas or methanol [8], but theoretically any substance capable of oxidation can be burned as fuel and fed to the anode. In this work, the term *fuel* refers to the matter which contains the hydrogen molecules. The fuel is in practice always used together with a solvent, for instance water. The electrolyte transports the hydrogen protons from the anode to the cathode, but also serves as a conductor, thus completing the electric circuit built up by the electrodes and the load. Moreover, it also prevents the fuel and oxidant from mixing. Fuel cells in which the fuel is mixed with the electrolyte are called *direct-mode fuel cells* [2]. [7]

Catalysts are used in fuel cells in order to provide sufficient power by boosting the reaction rates, particularly when operation occurs at low temperatures. Catalysts are placed on top of the anode and the cathode (see Fig. 2.1). Noble metals are widely used as catalysts, and platinum is the most active catalyst when operating with pure hydrogen as fuel. The main disadvantage of platinum is its high price; the month average in March 2011 was approximately 40 € per gram [11]. [5]

2.2 Fuel Cell Types

The most common classification of fuel cell types primarily considers the electrolytes used in the fuel cell. They include 1) the Alkaline Fuel Cell (AFC), 2) the Proton Exchange Membrane Fuel Cell (PEMFC), 3) the Direct Methanol Fuel Cell (DMFC), 4) the Phosphoric Acid Fuel Cell (PAFC), 5) the Molten Carbonate Fuel Cell (MCFC), and 6) the Solid Oxide Fuel Cell (SOFC). The fuel cell considered in this work can be classified as an AFC, but it has certain resemblance to the PEMFC. The fuel cell types can further be grouped into low-temperature fuel cells (AFCs, PEMFCs, DMFCs and PAFCs) or high-temperature fuel cells (MCFCs and SOFCs) [5]. Low-temperature fuel cells generally require catalysts in order to improve performance [5]. Next, the most common fuel cell types along with their distinctive features will be introduced. [6,8]

Alkaline Fuel Cells (AFCs) were proven to be viable sources of power already in the 1940's and were used to provide on-board electricity for the Apollo lunar flights [8]. The operation has traditionally occurred at pressures above 200 Pa and temperatures around 260 °C [7]. The AFC uses potassium hydroxide (KOH) as electrolyte, which typically is circulated around the fuel cell in order to be replaceable. This is due to the fact that the potassium hydroxide reacts with carbon dioxide in the air and changes to potassium carbonate. The advantages of alkaline fuel cells are the low overvoltage at the cathode, which decreases voltage losses, and fast chemical reactions, which enables the use of non-precious, low-cost materials without expensive platinum catalysts [12].

Mobile electrolytes also serve as a good cooling system since the circulating electrolyte effectively removes the heat from the system. Problems arise with the low reliability and durability which increases the price and makes the alkaline fuel cells economically unfeasible. Moreover, the problematic electrolyte conversion from hydroxide to carbonate has shifted the fuel cell development focus to non-alkaline fuel cells [10]. [6]

Proton Exchange Membrane Fuel Cells (PEMFCs), also known as *Polymer Electrolyte (Membrane) Fuel Cells*, were also developed for space vehicles. They are able to deliver high power densities, offering lower weight, cost and volume [7, 8]. The electrolyte consists of an immobilized, ion conduction polymer membrane which is bonded to the electrodes in such a manner that the anode, cathode and electrolyte form one very thin item [7]. Sulphonated fluoropolymers are the most commonly used electrolyte materials and among them a specific material developed by Dupont, Nafion$^{\circledR}$, is the most established one. The electrochemical function of the PEMFC is similar to the basic operation described in the beginning of the chapter (see (2.1) to (2.3)), that is, the proton exchange membrane transfers protons from the anode to the cathode, but without the presence of strong acids [8]. Another major advantage with polymer electrolytes is that they operate at low temperatures ($< 100\,^{\circ}$C). This allows faster startups and quick reactions to the change in power demand [7]. Other advantages include good sealing offered by the solid electrolyte membrane and that there are no corrosion problems [7, 12]. Due to low temperatures, platinum is required as a catalyst [12]. Another concern is the need for water in the polymer electrolyte in order to assure proton conductivity, which at temperatures below $100\,^{\circ}$C denotes handling water as a liquid. Water management in the membrane and electrodes is essential, because the membrane needs to be hydrated, while flooding the electrode pores must be avoided [5]. Currently, proton exchange membrane fuel cells are being developed for mobile use in cars and buses and for other portable applications. [6]

Direct Methanol Fuel Cells (DMFCs) operate similarly to the PEMFCs and comprise the same structure, electrolyte membrane and cathode reaction [12]. The anode reaction is however distinct since a mixture of water and methanol is used as fuel instead of hydrogen, which produces carbon dioxide as a by-product along with water [8, 12]. The main advantage of the direct methanol fuel cell is the use of liquid methanol which is easily stored compared to hydrogen. Methanol can also be manufactured from numerous basic substances and it can be used as fuel without reformation [8, 12]. Furthermore, methanol is a low-cost fuel with an energy density close to that of gasoline, and a direct methanol system is easy to use and quickly refillable [6]. Since the boiling point of methanol at 101.325 Pa (1 atm) is $65\,^{\circ}$C, the fuel cells operate at approximately $70\,^{\circ}$C. The main problem related to the DMFC is the slow proceeding of the anode reaction, because methanol reactions proceed much slower than hydrogen reactions [6]. This raises the need for suitable catalysts in order to excite the reactions [6, 8]. Another problem is

concerned with the fuel crossover, because methanol easily mixes with water [6]. Hence, a part of the methanol will reach the cathode without being split into protons and electrons, which causes inefficiency and lowers the cell voltage [6].

Phosphoric Acid Fuel Cells (PAFCs) also resemble PEMFCs due to their proton-conducting electrolytes. The PAFC operates approximately at temperatures from 180 to 200 °C and requires catalysts at both electrodes [8]. Phosphoric acid is used as the electrolyte, because it is the only common inorganic acid that exhibits the required thermal, chemical and electrochemical stability, and a volatility low enough to be used effectively. It is also tolerant to carbon dioxide contrary to the AFC. Due to the high operating temperature, some acid is lost during operation and has to be refilled. The PAFC uses gas diffusion electrodes and a mixture of carbon and platinum as catalysts. Phosphoric acid fuel cells can be combined in series to a stack of 50 or more cells. The PAFC was the first fuel cell technology that was commercially available, but the high costs within the technology set a large barrier for gaining economical competitiveness [7,8]. [6]

Molten Carbonate Fuel Cells (MCFCs) are high-temperature fuel cells, whose operating temperature is approximately 650 °C [7]. The electrolyte is a molten mixture of alkali metal carbonates, usually lithium and potassium or lithium and sodium carbonates. High temperatures are needed in order to reach sufficient conductivity of the electrolyte [7]. In contrast to all other fuel cell types, molten carbonate fuel cells require a supply of carbon dioxide to the cathode as well as oxygen. Due to high temperatures, precious catalysts are not needed in which case nickel and nickel oxide can be used to catalyze the reactions at the electrodes. MCFCs have been tested in power plants and are to be commercialized in the near future [8]. [6]

Solid Oxide Fuel Cells (SOFCs) are composed of only solid-state components and function at temperatures above 800 °C [7]. The electrolyte consists of an oxide ion-conducting ceramic material which eliminates the corrosion problems caused by liquid electrolytes [12]. The generated heat can be used as a by-product for other applications and the high operating temperature allows usage of non-noble catalysts, as is the case with the MCFC. The SOFC also possesses the ability to use a large variety of fuels, for instance hydrogen, carbon monoxide, methane, diesel, gasoline and coal gas, which makes it a promising technology [8]. The size is due to high temperatures not suited for smaller applications, but commercialization prospects in terms of power generation are promising [8]. [6]

2.3 Fuel Cell Fueling

Although hydrogen is preferred as the fuel due to its high reactivity and clean oxidation product (water), it does not appear naturally as gaseous fuel and has to be produced

artificially from some other source [6]. Next, we will discuss alternative methods for generating hydrogen, mainly out of fossil and biological fuels.

2.3.1 Fossil Fuels

Petroleum and *coal gas* are fossil fuels which are suitable for producing hydrogen. Petroleum consists of hydrocarbon-based chemical compounds in gaseous, liquid and solid form, which can be found in sedimentary rock deposits. Coal gas is very abundant with well-known properties that makes it a potential fuel for fuel cells [8]. However, fossil fuels are non-renewable sources of energy and emit carbon dioxide during reformation. [6]

Natural gas is also found inside porous rocks within the earth's crust. It is a mixture of hydrocarbons with traces of other gases, and varies greatly according to the source. Natural gas is also a by-product of several industrial processes and can be reformed to hydrogen as other fossil fuels [8]. Although natural gas is also a fossil fuel, the carbon dioxide emissions are lower than for petroleum and coal gas. [6]

2.3.2 Biofuels

Methanol can be mixed with potassium hydroxide (KOH) and used directly as a fuel and an electrolyte, respectively. It can also be mixed with water and used as fuel in direct methanol fuel cells, as described in Sec. 2.2. The advantages of methanol originate from the easy and low-cost manufacturing, trouble-free storage, high energy density and low operating temperature. The major problem when using methanol with an alkaline electrolyte is the reaction between the produced carbon dioxide and the electrolyte, forming harmful potassium carbonate which decreases the cell performance. [13]

Ethanol can be used similarly to methanol, by mixing it with an electrolyte. Both fuels also share the same main advantages. Compared to methanol, ethanol has the advantage that carbon dioxide is not created and hence no harmful carbonate can be formed. Nonetheless, the efficiency of ethanol is lower than that of methanol. [13]

Glucose can be produced from starch and cellulose by hydrolysis. From Fig. 2.2 we notice that fewer processing phases are required to produce glucose than bioethanol. Due to heat-consuming processes in ethanol production, it has a negative heat balance, while the heat balance for glucose is positive. Another advantage of glucose is that it in liquid phase can be used directly as a fuel in direct-mode fuel cells, mixed with the electrolyte. Liquid glucose is likewise easily stored as methanol and ethanol and more manageable compared to gaseous hydrogen. However, it is non-poisonous contrary to the alcohol fuels. The great interest towards glucose is due to the fact that producing

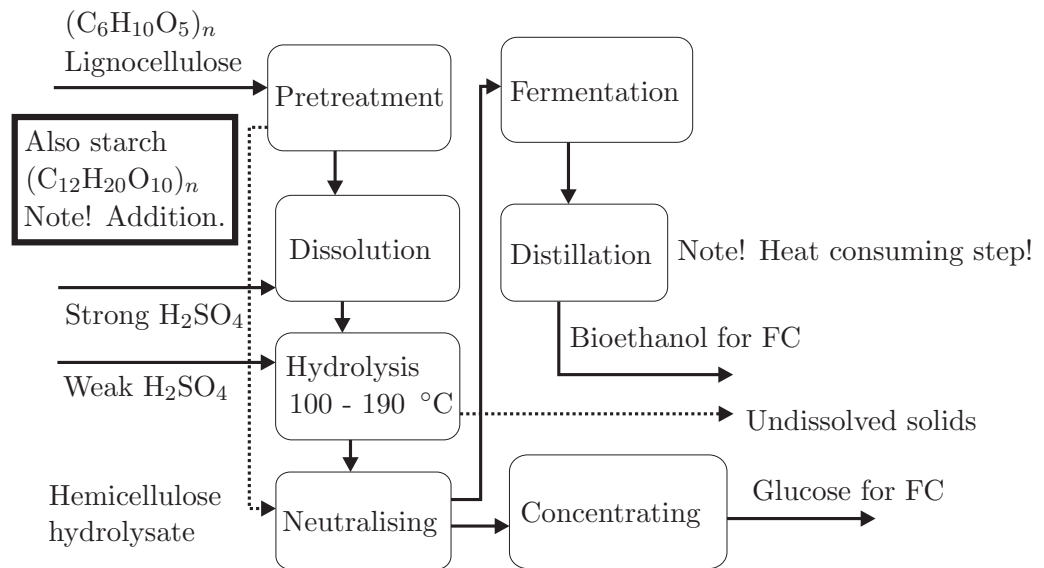for instance bioethanol requires more energy than a fuel cell driven by alcohol is able to generate. [1, 14]

Fig. 2.2: Principal flow chart of hydrolisation process [14].

2.4 Performance of a Fuel Cell

When comparing the performance of fuel cells, certain key figures are used. For the fuel cell electrodes and electrolytes, one of these figures is the current density of the fuel cell, given in $mAcm^{-2}$. The current density describes the current per unit area and should be reported along with a specific operating voltage, typically 0.6 to 0.7 V [5]. The current density also indicates the performance of the catalysts and their applicability in a specific fuel cell. [6]

A typical fuel cell polarization curve, which represents the cell voltage-current relationship and thus describes the fuel cell performance [15], is presented in Fig. 2.3 a). The highest voltage is the open-circuit voltage (OCV), which depends on the fuel concentration and the temperature [16]. The rapid voltage drop at low currents is caused by activation losses [8]. The polarization curve describes how the output voltage of a fuel cell varies when the load connected to the circuit, see Fig. 2.1, is altered [16]. While the load is decreased, the current increases and the output voltage decreases. The voltage value of 0.5 V is the lowest value of the alkaline fuel cell, because below that voltage the alkaline electrolyte begins to penetrate into the cathode, which damages the fuel cell [4]. The power-current curve, corresponding to the voltage-current curve, is presented in Fig. 2.3 b). At different currents the available power differs, and the maximum power should be found at a current level lower than the maximum [17]. From Fig. 2.3 a) it can
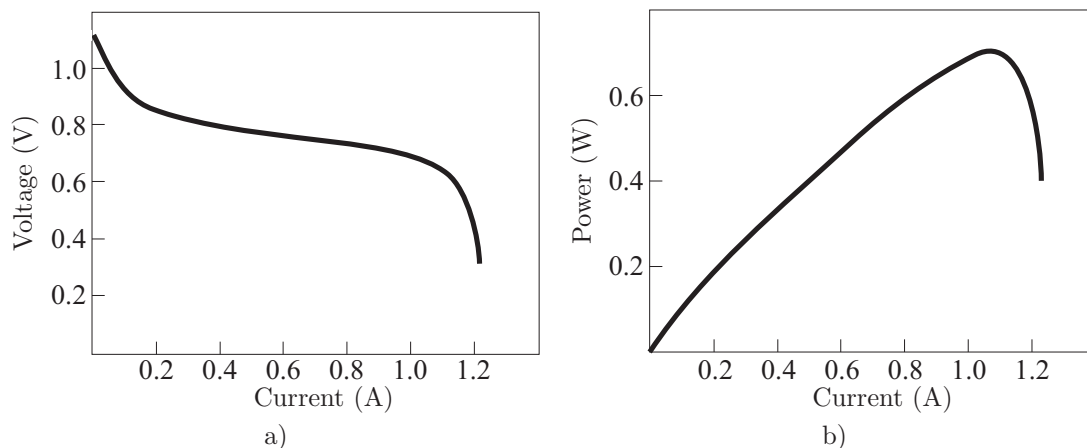
Fig. 2.3: a) Typical polarization curve of a fuel cell [5] and b) its corresponding power-current curve.

be seen that at a certain current, the voltage drops rapidly. The operating voltage is usually a compromise between the maximum power density and the maximum current density, which cannot be obtained simultaneously [5]. Below this specific voltage value the power density value begins to decrease rapidly because of limitations in the operation of the cathode and anode electrodes [17]. In the alkaline direct-mode glucose fuel cell studied in this work the maximum power density has been detected to be at the current level which corresponds to a voltage value between 0.5 and 0.6 V [17].

Direct fuel cells supplied with hydrogen or alcohols may reach current densities of several hundred $mAcm^{-2}$, while direct-mode glucose fuel cells are only able to produce levels from 5 to 8 $mAcm^{-2}$ [2]. AFCs typically obtain current densities of 100 to 200 $mAcm^{-2}$. However, the Apollo shuttles, that are based on alkaline fuel cells as mentioned in Sec. 2.2, operated at much higher current densities (470 $mAcm^{-2}$) [7]. PAFCs operate at current densities in the range of 150-400 $mAcm^{-2}$ at cell voltages from 600 to 800 mV [6, 7]. MCFCs operate at current densities in the range of 100 to 200 $mAcm^{-2}$ [7]. SOFCs operate at current density ranges around 200 $mAcm^{-2}$ [7]. PEMFCs have subsequent to various development increased the current densities to over 1000 $mAcm^{-2}$ [6].

2.5 Fuel Cell Efficiency Enhancement by Means of Electromagnetic Fields

The direct-mode fuel cells have very low current densities when using glucose as the fuel. The oxidation reaction is capable of yielding only two electrons per one molecule from 24 available electrons [14]. By feeding an electromagnetic field into a cylindrical fuel cell, the efficiency of the fuel cell may be enhanced [2]. The current densities have been reported to increase from 8 to 13 $mAcm^{-2}$ when DC signals are fed into the fuel cell

from the function generator [2]. At 5 MHz frequency the current densities have been reported to increase above 13 mAcm^{-2} [3].

It is expected that this current density value of the direct-mode fuel cell is increased even from the current maximum value of 15 mA cm^{-2} when the number of the extracted electrons will increase from the current maximum values of two electrons per one glucose molecule towards the maximum of 24 electrons per one glucose molecule [2, 4].

In previous research, a current capacity of 25836 Coulombs (As) has been reported [3]. The available charge can be calculated with [18]

$$Q = F \, n_e V_{an} C_0, \tag{2.4}$$

where F is the Faraday constant, n_e is the number of electrons transferred, V_{an} is the volume of liquid in the anode and C_0 is the glucose concentration. The equation yields 57900 As, when $n_e = 2$, $V_{an} = 0.3$ dm^3 and $C_0 = 1$ Mol/dm^3. This is the theoretical capacity of the fuel cell under test, when two electrons are extracted per one glucose molecule.

CHAPTER 3

Coaxial Cable Theory

The fuel cell investigated in this work behaves electromagnetically as a coaxial cable due to the cylindrical shape of the fuel cell, as seen in Fig. 3.1. Because the fuel cell will be fed with precisely known electromagnetic fields, basic knowledge of the electromagnetic behavior of coaxial cables is essential. In this chapter, the properties of the coaxial cable will be presented, beginning with Maxwell's equations, waveguide basics and the cable structure. Also multi-layered dielectrics will be discussed.
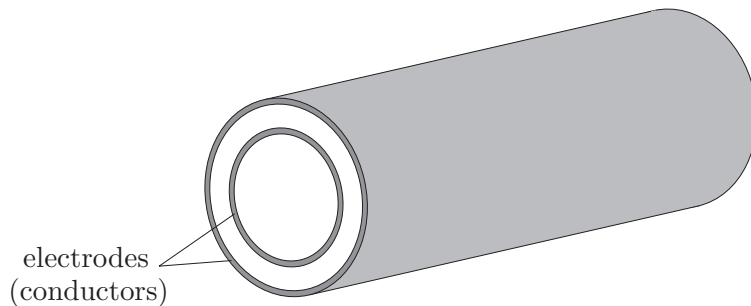

Fig. 3.1: Structure of the fuel cell investigated in this work.

3.1 From Maxwells's Equations to the Helmholtz Equation

Electromagnetism, as a science, is fundamentally based on Maxwell's equations [19], which essentially are based on empiric knowledge and theory developed by other scientists in the field [20]. They also offer a historical view into radio science, whose development is easier to comprehend by knowing the most famous work of Maxwell. Maxwell's equations in differential form can be written as follows [20, 21]:

$$\nabla \cdot \vec{D} = \rho, \tag{3.1}$$

$$\nabla \cdot \vec{B} = 0, \tag{3.2}$$

$$\nabla \times \vec{E} = -\frac{\partial \vec{B}}{\partial t}, \tag{3.3}$$

$$\nabla \times \vec{H} = \vec{J} + \frac{\partial \vec{D}}{\partial t}, \tag{3.4}$$

where the vector differential operator $\nabla = \frac{\partial}{\partial x}\hat{x} + \frac{\partial}{\partial y}\hat{y} + \frac{\partial}{\partial z}\hat{z}$, D is the electric flux density, ρ is the electric charge density, B is the magnetic flux density, E is the electric field, H is the magnetic field and J is the current density. The relationship between the fields and the flux and current densities are [19–21]:

$$\vec{J} = \sigma \vec{E}, \tag{3.5}$$

$$\vec{D} = \varepsilon \vec{E}, \tag{3.6}$$

$$\vec{B} = \mu \vec{H}, \tag{3.7}$$

where σ is the conductivity, ε is the permittivity and μ is the permeability of the medium. A dielectric is called *isotropic* when the properties are the same in every direction. The characteristics of a *linear* dielectric are independent on changing field strengths. If the dielectric is isotropic and linear and the derivatives are approximated as time-harmonic, the Maxwell equations simplify to [20, 21]:

$$\nabla \cdot \vec{E} = 0, \tag{3.8}$$

$$\nabla \cdot \vec{H} = 0, \tag{3.9}$$

$$\nabla \times \vec{E} = -\mathrm{j}\omega\mu\vec{H}, \tag{3.10}$$

$$\nabla \times \vec{H} = \mathrm{j}\omega\varepsilon\vec{E}, \tag{3.11}$$

where $\omega = 2\pi f$ is the angular frequency and f is the frequency. When multiplying (3.10) with the operator $\nabla\times$ and using (3.8), (3.11) and the vector calculus theorem [21]

$$\nabla \times \nabla \times \vec{A} = \nabla(\nabla \cdot \vec{A}) - \nabla^2\vec{A}, \tag{3.12}$$

we attain the equation [20, 21]

$$\nabla^2\vec{E} = -\omega^2\mu\varepsilon\vec{E} = -k^2\vec{E}, \tag{3.13}$$

called the Helmholtz equation, where $k = \omega\sqrt{\mu\varepsilon}$ is called the wave number.

Assuming that the electric field varies only in the x direction, the wave will propagate

in the z direction and the Helmholtz equation simplifies to [20, 21]

$$\frac{\partial^2 E_x}{\partial z^2} + k^2 E_x = 0. \tag{3.14}$$

The solution for the equation is [20, 21]

$$E_x(z) = E^+ e^{-\mathrm{j}kz} + E^- e^{\mathrm{j}kz}, \tag{3.15}$$

where E^+ and E^- are arbitrary amplitude constants whose values are determined from the boundary conditions.

3.2 Basic Waveguide Equations

Since the medium within waveguides is source free, the Helmholtz equation applies [20, 21]. If it is assumed that waves propagate in the z direction and the z-dependence is related to $e^{-\gamma z}$, the electric field can be represented by [21]

$$\vec{E} = \vec{E}(x, y, z) = \vec{g}(x, y)e^{-\gamma z}, \tag{3.16}$$

where γ is the propagation constant. When this equation is inserted in the Helmholtz equation (3.13), the following equation is obtained [21]:

$$\nabla^2 \vec{E} = \nabla^2_{xy}\vec{E} + \frac{\partial^2 \vec{E}}{\partial z^2} = \nabla^2_{xy}\vec{E} + \gamma^2 \vec{E} = -\omega^2 \mu\varepsilon\vec{E}, \tag{3.17}$$

where ∇^2_{xy} expresses a partial derivative for x- and y-directions. Similar equations can also be written for the magnetic fields, yielding two equations which apply for all straight wave guides [21]:

$$\nabla^2_{xy}\vec{E} = -(\gamma^2 + \omega^2 \mu\varepsilon)\vec{E}, \tag{3.18}$$

$$\nabla^2_{xy}\vec{H} = -(\gamma^2 + \omega^2 \mu\varepsilon)\vec{H}. \tag{3.19}$$

The transverse components E_x, E_y, H_x and H_y can be written as functions of E_z and H_z [20, 21]:

$$E_x = \frac{-1}{\gamma^2 + \omega^2 \mu\varepsilon} \left(\gamma\frac{\partial E_z}{\partial x} + \mathrm{j}\omega\mu\frac{\partial H_z}{\partial y} \right), \tag{3.20}$$

$$E_y = \frac{1}{\gamma^2 + \omega^2 \mu\varepsilon} \left(-\gamma\frac{\partial E_z}{\partial y} + \mathrm{j}\omega\mu\frac{\partial H_z}{\partial x} \right), \tag{3.21}$$

$$H_x = \frac{1}{\gamma^2 + \omega^2 \mu\varepsilon} \left(\mathrm{j}\omega\varepsilon\frac{\partial E_z}{\partial y} - \gamma\frac{\partial H_z}{\partial x} \right), \tag{3.22}$$

$$H_y = \frac{-1}{\gamma^2 + \omega^2 \mu\varepsilon} \left(\mathrm{j}\omega\varepsilon\frac{\partial E_z}{\partial x} + \gamma\frac{\partial H_z}{\partial y} \right). \tag{3.23}$$

3.3 TEM Waves

TEM-waves are the desired waveform in coaxial cables [21]. The electric field E and the magnetic field H are thus perpendicular to the direction of propagation and we have $E_z = 0$ and $H_z = 0$. Therefore, when regarding (3.20) to (3.23), the x- and y-components must also be zero, unless [21]

$$\gamma^2 + \omega^2 \mu \varepsilon = 0. \tag{3.24}$$

For TEM mode, the propagation constant γ can be calculated as [21]

$$\gamma = \pm j\omega\sqrt{\mu\varepsilon} \approx \pm j\omega\sqrt{\mu}\operatorname{Re}\{\sqrt{\varepsilon}\} = \pm j\frac{2\pi}{\lambda} = \pm j\beta, \tag{3.25}$$

when the losses are considered to be low, where β is the wave number and λ is the wavelength, which can be calculated from [21]

$$\lambda = \frac{1}{f\sqrt{\mu\varepsilon}}. \tag{3.26}$$

The phase velocity v_p is [20]

$$v_p = \frac{\omega}{\beta} = \frac{1}{\sqrt{\mu\varepsilon}}. \tag{3.27}$$

When $\varepsilon = \varepsilon_0$ and $\mu = \mu_0$, where ε_0 and μ_0 are the permittivity and permeability in vacuum, respectively, v_p is the speed of light c. We attain the TEM mode wave equations as [21]

$$\nabla_{xy}^2 \vec{E} = 0, \tag{3.28}$$

$$\nabla_{xy}^2 \vec{H} = 0. \tag{3.29}$$

The waves propagating towards z direction satisfy the equation [21]

$$\frac{E_x}{H_y} = -\frac{E_y}{H_x} = \eta, \tag{3.30}$$

where $\eta = \sqrt{\mu/\varepsilon}$ is the wave impedance. The electric field can also be written as the gradient of the scalar potential [21]:

$$\vec{E}(x,y) = -\nabla_{xy}\Phi(x,y). \tag{3.31}$$

In an uncharged environment Maxwell's first equation (3.8) states, that $\nabla \cdot \vec{E} = \varepsilon\nabla_{xy} \cdot \vec{E} = 0$, which combined with Eq. (3.31) leads to the Laplace equation [21]:

$$\nabla_{xy}^2 \Phi(x,y) = 0. \tag{3.32}$$

The voltage between the inner and outer conductor is [20, 21]

$$V_{12} = -\int_1^2 \vec{E} \cdot \vec{dl} = \Phi_1 - \Phi_2, \tag{3.33}$$

where 1 and 2 are the first and second conductor, respectively, and Φ_1 and Φ_2 are the conductor potentials. The current is according to Ampère's law [20, 21]

$$I = \oint_\Gamma \vec{H} \cdot \vec{dl}, \tag{3.34}$$

where Γ is the cross-sectional contour of the conductor. TEM modes can occur only in waveguides with two or more conductors.

3.4 Coaxial Cables

The coaxial cable is the most widely used transmission line for transferring RF (Radio Frequency) energy and it is very broadband [22]. Its shielded structure prevents the cable from interfering with other devices and external fields from coupling into the line [23–25]. This is due to the outer conductor, which, if ideally conducting, will not permit fields from penetrating through it [20, 24]. The fundamental mode inside coaxial cables is TEM [21, 22].

3.4.1 Structure of the Coaxial Cable

A coaxial cable is a shielded waveguide which consists of a cylinder shaped outer conductor and a thinner inner conductor, both sharing the same geometric axis (see Fig. 3.2) [21, 23]. There is an insulating layer between the two conductors, designated the dielectric, which electrically separates the conductors from each other and provides the cable a stable form [23, 26]. The conductivities and permittivities of the conductors and the isolator along with the cable dimensions define the electric properties of the coaxial cable. The cable is typically protected from moisture, dust et cetera by a plastic outer jacket which does not affect the electric properties [22]. [21]

The inner and outer conductors are made of copper, steel or aluminum and can also be plated with a highly conductive metal such as silver [26]. The inner conductor can be a solid or stranded cylinder. Popular insulators are polyethylene, polypropylene, PTFE (Teflon) and organic polymers [22, 24, 27].
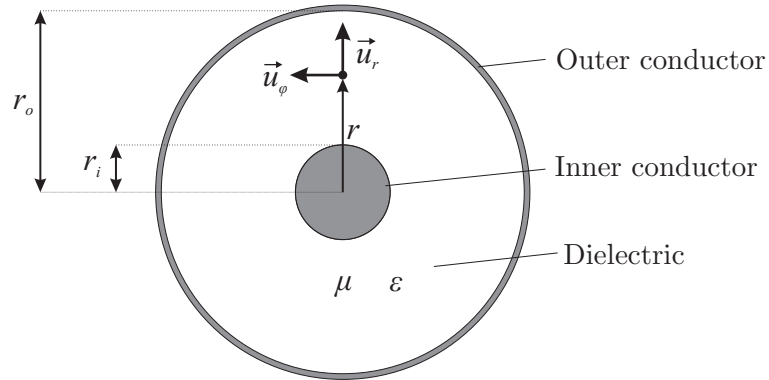
Fig. 3.2: Cross-section of a coaxial cable.

3.4.2 Different Types of Coaxial Cables

Coaxial cables are categorized depending on the cable stiffness. Depending on the usage purpose cables are made either flexible, semi-rigid or rigid. The rigidity affects the electrical properties.

Flexible cables have the lowest electrical properties due to their braided conductors and elastic dielectrics [22, 23]. The braided outer conductor possesses lower conductivity than a solid conductor and the slots allow electromagnetic fields to penetrate through the conductor. Semi-rigid cables are stiffer due to the solid outer conductor, but they are not intended to be bent frequently due to the and the electrical properties are better compared to flexible cables [22].

Rigid coaxial cables are inflexible with very stable electrical properties [23]. The fuel cell studied in this work resembles a rigid cable although it has certain resemblance to the semi-rigid cable due to the small slots in the outer conductor.

3.4.3 Equations for Coaxial Cables

In coaxial cables, the wave mode is TEM and the fields can be derived from Laplace's equation (3.32) as [21]:

$$\frac{1}{r}\frac{\partial}{\partial r}\left(r\frac{\partial \Phi(r,\phi)}{\partial r}\right) + \frac{1}{r^2}\frac{\partial^2 \Phi(r,\phi)}{\partial \phi^2} = 0, \tag{3.35}$$

where r is the radius. By regarding the boundary conditions $\Phi(r_o,\phi) = 0$ and $\Phi(r_i,\phi) = V$ the potential can be solved as [21]

$$\Phi(r,\phi) = V\frac{\ln(r_o/r)}{\ln(r_o/r_i)}. \tag{3.36}$$

Hence, the electric field is [20, 21]

$$\vec{E}(r, \phi) = -\nabla\Phi(r, \phi) = \vec{u}_r \frac{V}{\ln(r_o/r_i)} \frac{1}{r}, \tag{3.37}$$

where $\vec{u}_r$ is a unit vector directed along the radius. The magnetic field can be solved similarly as [20, 21]

$$\vec{H}(r, \phi) = \frac{1}{\eta}\vec{u}_z \times \vec{E}(r, \phi) = \vec{u}_\phi \frac{V}{\eta r \ln(r_o/r_i)} = \vec{u}_\phi \frac{I}{2\pi r}, \tag{3.38}$$

where I is the current in the inner conductor, $\vec{u}_z$ is a unit vector directed along the z-axis and $\vec{u}_\phi$ is the unit vector orthogonal to $\vec{u}_r$. The voltage between the conductors is [28]

$$V = -\int_{r_o}^{r_i} \frac{q}{2\pi\varepsilon r} \, dr = \frac{q}{2\pi\varepsilon} \ln\left(\frac{r_o}{r_i}\right), \tag{3.39}$$

where q is the electric charge, and r_i and r_o are the radii of the inner and outer conductors, respectively (Fig. 3.2). From this we can calculate the capacitance per unit length as [20, 28]

$$C_l = \frac{q}{V} = \frac{2\pi\varepsilon}{\ln\left(\frac{r_o}{r_i}\right)}. \tag{3.40}$$

The inductance and conductivity per unit length, respectively, are [20, 21, 28]

$$L_l = \frac{\mu}{2\pi} \ln\left(\frac{r_o}{r_i}\right), \tag{3.41}$$

$$\sigma_l = \frac{\sigma}{\varepsilon} c = \frac{2\pi\sigma}{\ln\left(\frac{r_o}{r_i}\right)}. \tag{3.42}$$

The characteristic impedance of a coaxial cable can be calculated from $V = IZ$ and expanded to [20, 21]

$$Z_0 = \frac{V}{I} = \frac{\eta}{2\pi} \ln(r_o/r_i) = \sqrt{\frac{\mu}{\varepsilon}} \frac{\ln(r_o/r_i)}{2\pi}. \tag{3.43}$$

There is a cable loss due to the finite conductivity of the conductors and unideal properties of the dielectric. The attenuation factor due to conductor loss can be calculated with [20, 21]

$$\alpha_c = \frac{R_s}{4\pi Z_0} \left(\frac{1}{r_o} + \frac{1}{r_i}\right), \tag{3.44}$$

when both conductors have the same surface resistance R_s. The attenuation constant for the dielectric loss is [20, 21]

$$\alpha_d = \frac{\pi}{\lambda} \tan \delta, \tag{3.45}$$

where $\tan \delta$ is the loss tangent of the insulator. The equation is valid if $\tan \delta << 1$. In order to prevent higher order TE and TM modes from propagating in the coaxial cable, the wavelength λ inside the cable must satisfy [21]

$$\lambda > \pi(r_o + r_i). \tag{3.46}$$

3.5 Wave Propagation in Coaxial Cables with Multi-layered Dielectrics

When the insulator in the coaxial cable consists of several dielectric layers with different electrical properties (Fig. 3.3), the evaluation of the cable properties becomes more complicated. Now, the characteristic impedance of the cable changes compared to the case where the insulator is homogeneous.
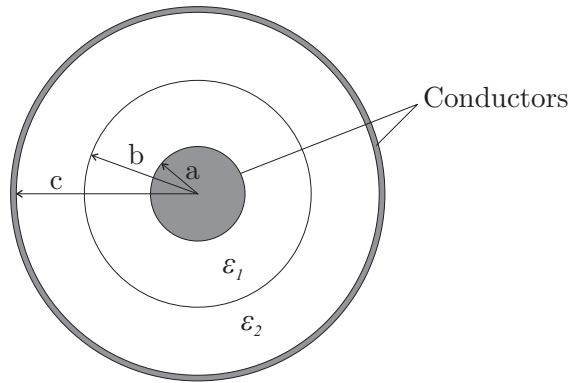

Fig. 3.3: Cross-section of a coaxial cable with two dielectric layers.

The characteristic impedance Z_0 for any TEM waveguide can be calculated with [20, 29]:

$$Z_0 = \sqrt{\frac{L_l}{C_l}}. \tag{3.47}$$

Since the inductance per unit length L_l is independent of the permittivity ε (3.41), it is not affected by the different dielectric properties in the insulator layers, assuming that the materials are non-magnetic ($\mu = \mu_0$) [30]. By contrast the capacitance per unit length C_l does depend on the permittivity (3.40), and a changing capacitance also alters the characteristic impedance. Each insulator layer can be seen as a single capacitor, hence, the layers can be seen as capacitors connected in series [30] and the total capacitance per unit length C_{lT} can be calculated with [31]:

$$\frac{1}{C_{lT}} = \frac{1}{C_1} + \frac{1}{C_2} + \frac{1}{C_3} + \dots, \tag{3.48}$$

where $C_1, C_2, C_3, \dots$ are the capacitances of the single capacitors. With a double dielec-

tric the total capacitance per unit length is

$$\frac{1}{C_T} = \frac{1}{C_{ab}} + \frac{1}{C_{bc}}, \tag{3.49}$$

where C_{ab} is the capacitance per unit length of the inner dielectric (permittivity ε_1) and C_{bc} the capacitance per unit length of the outer dielectric (permittivity ε_2), see Fig. 3.3.

The total capacitance per unit length of a double dielectric coaxial cable can be calculated with (3.40) and (3.49). We attain the following equation:

$$C_T = \frac{2\pi\varepsilon_1\varepsilon_2}{\varepsilon_1 \ln\left(\frac{c}{b}\right) + \varepsilon_2 \ln\left(\frac{b}{a}\right)}, \tag{3.50}$$

where a is the radius of the inner conductor, b the radius of the dielectric boundary surface and c the radius of the outer conductor. The total inductance per length unit is calculated with (3.41), where $\mu = \mu_0$, and as the capacitance per unit length is known from (3.40), the characteristic impedance for a double dielectric coaxial cable can be calculated from (3.47):

$$Z_0 = \sqrt{\frac{\mu_0 \ln(c/a)}{2\pi} \cdot \frac{\varepsilon_1 \ln\left(\frac{c}{b}\right) + \varepsilon_2 \ln\left(\frac{b}{a}\right)}{2\pi\varepsilon_1\varepsilon_2}} = \frac{1}{2\pi}\sqrt{\mu_0 \ln\left(\frac{c}{a}\right)\left(\frac{\ln\left(\frac{c}{b}\right)}{\varepsilon_2} + \frac{\ln\left(\frac{b}{a}\right)}{\varepsilon_1}\right)}. \tag{3.51}$$

Similarly, equations can be derived for cables with several dielectrics by calculating the capacitance for each layer individually and utilizing (3.47) and (3.48).

The effective relative permittivity ε_{eff} for the dual dielectric waveguide is obtained by dividing the total capacitance C_T by the capacitance of a similar air-filled waveguide [29, 30]:

$$\varepsilon_{eff} = \frac{\varepsilon_1\varepsilon_2 \ln(c/a)}{\varepsilon_0(\varepsilon_1 \ln\left(\frac{c}{b}\right) + \varepsilon_2 \ln\left(\frac{b}{a}\right))} = \frac{\varepsilon_{1,r}\varepsilon_{2,r} \ln(c/a)}{\varepsilon_{1,r} \ln\left(\frac{c}{b}\right) + \varepsilon_{2,r} \ln\left(\frac{b}{a}\right)}, \tag{3.52}$$

where $\varepsilon_{1,r}$ and $\varepsilon_{2,r}$ are the relative permittivities of the two dielectric layers. Here, the waveform inside the cable cannot be TEM due to the fact that the propagation constant is different in the two dielectrics. However, if the deviation from a perfect TEM-mode is small, the waveform is called quasi TEM (QTEM). [30]

CHAPTER 4

CONFIGURATION AND ELECTRICAL PROPERTIES OF THE FUEL CELL

4.1 Fuel Cell Configuration

The fuel cell under test is a direct-mode bioorganic fuel cell in which the fuel and the alkaline electrolyte are mixed with each other. Hence, the fuel cell belongs to the class of alkaline fuel cells. A picture of the fuel cell is presented in Fig. 4.1. The fuel cell uses monosaccharide glucose ($C_6H_{12}O_6$) soluted in battery water (distilled water) as fuel and potassium hydroxide (KOH) as the electrolyte. The anode catalyst consists of Raney nickel and at the cathode the catalyst consists of pyrolized cobalt porphyrin complex (CoTPP) on carbon together with spinel ($MnCo_2O_4$). It can be noted that the
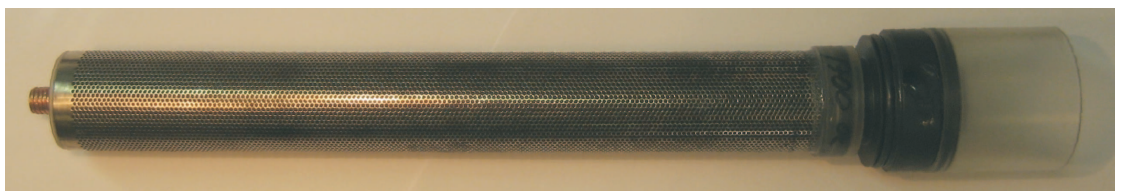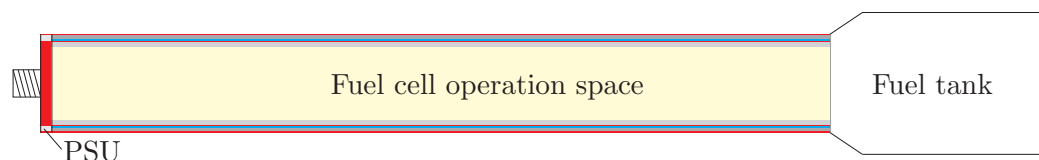

Fig. 4.1: The fuel cell under test.

Fig. 4.2: Simplified illustration of the fuel cell.

electrolyte and the catalyst materials can be changed from one test model to another,

---

and the above-mentioned materials apply for the fuel cell model which was used during the material and output power measurements.

A simplified illustration of the fuel cell is shown in Fig. 4.2. The fuel cell operation space, where the reactions take place, occupies the largest part of the fuel cell. The length of this part is approximately 22 cm. In order to keep the fluids in place, there is a plastic plug at the left end of the fuel cell. This piece, made out of polysulfone (PSU), has a length of 3 mm. At the other end of the fuel cell, there is a fuel tank, which assists the filling of the fuel. The fuel cell is kept vertically during operation and thus a plug is required only at the bottom (left end in Figs. 4.1 and 4.2).

The cross-section of the operational part of the fuel cell is presented in Fig. 4.3. The outer layer, the cathode, is perforated nickel-plated copper, which is an excellent electrical conductor (conductivity for annealed copper at $20\,°C$ is 58 MS/m [32]) and the holes, approximately 1 mm in diameter, allow oxygen to penetrate through the layer. It is noted, that the holes have a small influence on the conductivity. Within the outer layer is a porous layer composed of carbon, Teflon and the cathode catalyst, which allows the oxygen to penetrate through this layer as well. For simplicity, this layer is designated as CTC. Going inwards radially, the next layer is composed of battery water with a variable concentration of glucose, which is denominated the fuel solution. Next to the fuel solution, as the fourth layer, is a similar perforated nickel-plated copper layer as the outer layer. Certain models also have a layer of acid-proof steel on top of the copper. This copper tube is the fuel cell anode. The layer closest to the fuel space in the middle of the fuel cell is composed of porous Raney nickel and functions as a catalyst for the anode. The layer thicknesses are presented in Table 4.1.
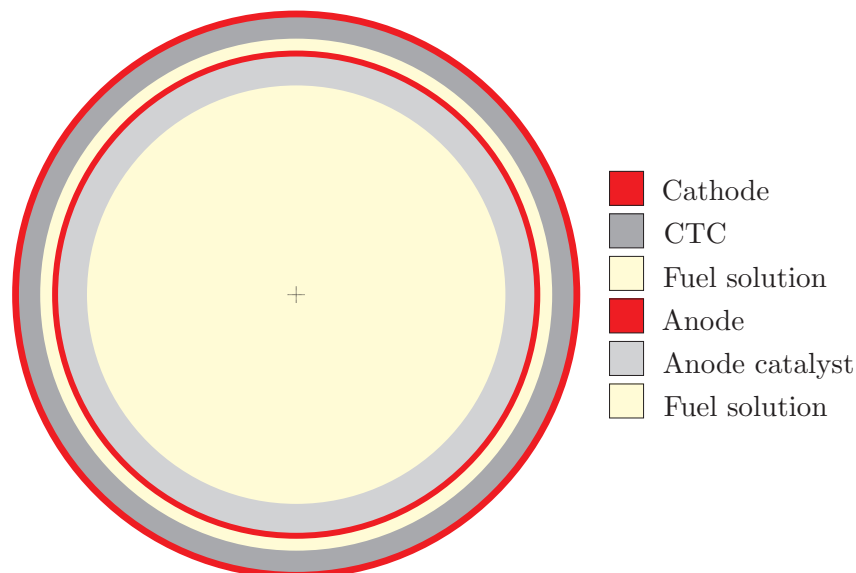

Fig. 4.3: Cross-section of the fuel cell.

Table 4.1: Order and thickness of the fuel cell layers.

	Material	Outer diameter [mm]	Inner diameter [mm]	Layer thickness [mm]
1.	Cathode (Ni-Cu)	33.4	32.6	0.4
2.	CTC (Carbon + Teflon + CoTPP + $MnCo_2O_4$)	32.6	30.1	1.25
3.	Fuel solution (H_2O + glucose + KOH)	30.1	28.7	0.7
4.	Anode (Ni-Cu)	28.7	28.0	0.35
5.	Anode catalyst (Raney-Ni)	28.0	24.6	1.7
6.	Fuel solution (H_2O + glucose + KOH)	24.6	-	-

The fuel solution (glucose and KOH soluted in battery water), fed into the middle of the fuel cell, penetrates through the Raney nickel layer (fifth layer) and the porous nickel-plated copper tube (fourth layer) to the space (third layer) between the CTC and the anode. The fuel solution penetrates approximately halfway into the CTC layer.

4.2   Waveguide Characteristics of the Fuel Cell

The studied fuel cell operates electrically as a coaxial cable due to its cylindrical shape with a coaxial structure, the metallic electrodes and the dielectric between the conductors. This is seen by comparing Figs. 3.2, 3.3 and 4.3.

Essentially, the insulator consists of two layers which may be dielectric: the CTC and the fuel solution layer. However, these layers can also act as conductors, and as described previously in Sec. 4.1, the substance inside the layers is not homogeneous. Therefore, treating the layers theoretically as in Sec. 3.5 should be made with reservation. In order to specify the dielectric properties of these layers, permittivity measurements have to be conducted. The measurements are reported in Sec. 4.3.

4.2.1   Permittivity of the Cable Dielectric

The permittivity of a coaxial cable dielectric can be considered as the most important property, because it enables calculation of many important electrical properties of the cable, such as the characteristic impedance and attenuation. The permittivity is also

required in order to construct an accurate simulation model. The complex permittivity ε of a material can be defined as [21, 33]

$$\varepsilon = \varepsilon_r \varepsilon_0 = \varepsilon^{'} - \mathrm{j}\varepsilon^{''} = \varepsilon^{'}(1 - \mathrm{j}\tan\delta), \tag{4.1}$$

where ε_r is the relative permittivity of the medium, $\varepsilon_0 = 8.854 \times 10^{-12}$ is the permittivity of vacuum and $\varepsilon^{'}$ and $\varepsilon^{''}$ are the real and imaginary parts of the permittivity, respectively. The imaginary part is a measure of how dissipative a medium is and affects thus the attenuation for a wave propagating in the medium [33]. In this definition, both polarization and conduction losses are included in $\varepsilon^{''}$ [21], which in reality is defined as [33]

$$\varepsilon^{''} = \varepsilon_d^{''} + \frac{\sigma}{\omega}, \tag{4.2}$$

where $\varepsilon_d^{''}$ represents the dielectric losses and σ/ω the conductivity losses. In order to calculate the dielectric loss (3.45), the loss tangent and the wavelength inside the dielectric are required. The definition of the loss tangent can be obtained from Eq. (4.1) to be [22, 33]

$$\tan\delta = \frac{\varepsilon^{''}}{\varepsilon^{'}} = \frac{\varepsilon_r^{''}}{\varepsilon_r^{'}}, \tag{4.3}$$

where $\varepsilon_r^{'}$ and $\varepsilon_r^{''}$ are the real and imaginary parts of the relative permittivity, respectively. If this complex permittivity is placed in Eq. 3.25, the propagation constant becomes

$$\gamma = \pm\mathrm{j}\omega\sqrt{\mu\varepsilon} = \pm\mathrm{j}\frac{2\pi}{\lambda}\sqrt{1 - \tan\delta} = \mathrm{j}\beta + \alpha, \tag{4.4}$$

where α is the attenuation constant. The wavelength λ inside a medium can be calculated from [33]

$$\lambda = \frac{\lambda_0}{\mathrm{Re}(\sqrt{\varepsilon_r})}, \tag{4.5}$$

where λ_0 is the wavelength in vacuum. Hence, determining permittivity is essential for calculating dielectric properties. If it is assumed that the losses in (4.2) are entirely conductivity losses, the conductivity is [21]

$$\sigma = \varepsilon_0 \varepsilon_r^{''} \omega. \tag{4.6}$$

4.3 Permittivity Measurements

In order to measure the permittivity of a dielectric material, many methods can be used, for instance the lumped circuits method, the resonance method, the transmission line propagation method or the free-space propagation method [33]. In this work the transmission line propagation method is used, and the permittivities of the most important

fuel cell materials are measured with an HP 8753D network analyzer and an HP 85070A dielectric probe kit. The dielectric probe is an open-ended coaxial line, which is one of the most common permittivity measurement methods [33, 34]. The frequency range of the probe extends from 0.2 to 20 GHz with a ±5% uncertainty in permittivity of the material under test [34, 35]. The device is suited for measuring liquid and solid samples, and the assisting software facilitates the measurements. An illustration of the probe is shown in Fig. 4.4.
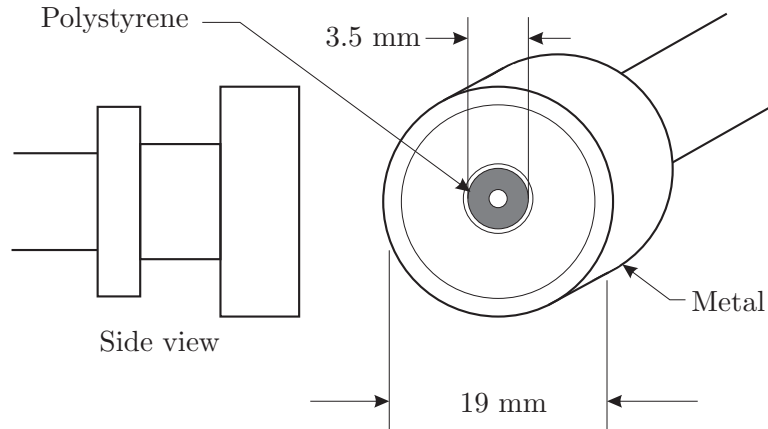

Fig. 4.4: HP 85070A Dielectric probe [34].

4.3.1   Operating Principle of the Dielectric Probe Kit

The dielectric probe kit is composed of the probe and a software. The software requires a Windows operating system and certain features of the computer, but due to the age of the software the computer qualifies easily. The only required accessory is a GPIB card inside the computer. The computer is connected via the GPIB interface to the compatible network analyzer (8753D), and the probe is connected to the input port of the analyzer. No calibration of the network analyzer is needed, however the software calibrates the probe with three known measurements; air, a metallic short and deionized water [34, 35]. After this the probe is calibrated and ready for use. The permittivity range of the probe extends from 2.5 to 80.

The dielectric probe is essentially an open-ended coaxial line, as mentioned earlier. Liquid materials can be easily and accurately measured, because the contact is strict and no air gaps are formed between the probe and the measured material, which is required in order to avoid large measurement errors [33, 34]. For solid materials measuring is more inaccurate because avoiding air gaps can be almost impossible. Another requirement is that the thickness of the material exceeds $20/\sqrt{|\varepsilon_r|}$ mm, otherwise the field penetrates through the material under test which distorts the result [33, 34].

The operation of the dielectric probe is illustrated in Fig. 4.5. A discontinuity arises between the probe and the material under test [33], which causes a measurable amount of power to reflect at the material interface towards the source, which will be discussed in more detail in Sec. 5.1. The reflection coefficient calculated in the analyzer defines the properties of the material under test. The software outputs real and imaginary parts of the relative permittivity.
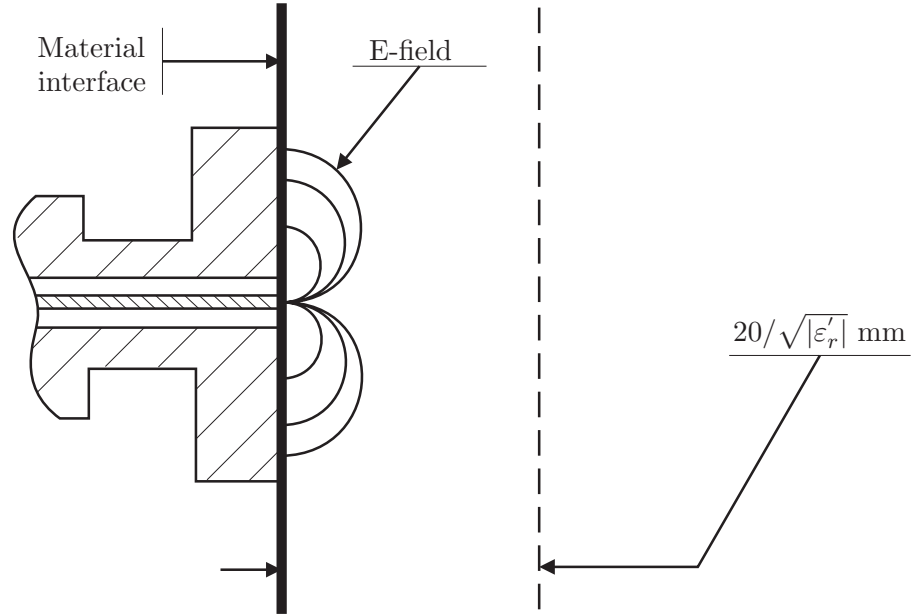

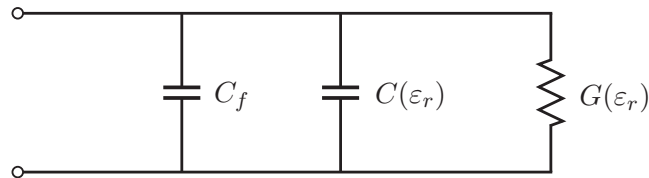Fig. 4.5: Interaction region of the electric field of the dielectric probe [34].

Fig. 4.6: Equivalent circuit for the open-ended coaxial probe [33].

The real part ε_r' of the material under test influences the phase of the reflected wave and the imaginary part of the permittivity, ε_r'', influences the amplitude. The open-ended coaxial cable probe measurement can be characterized by the equivalent circuit in Fig. 4.6, where G is the radiation conductance, C_f is the capacitance of the field inside the sensor, and C is the capacitance of the field outside the sensor (inside the material under test). C and G depend on both the permittivity of the sample and the coaxial cable dielectric, and also on the dimensions of the transmission line. C_f depends only on the cable properties. [33]

For air, which is one of the calibration materials, the values $G = G_0$, $C = C_0$ and C_f can be calculated analytically or measured. A simple approximation neglects C_f, G_0 and G,

and the reflection coefficient can be calculated as

$$\rho_L = \frac{-Z_0 + 1/[j\omega C_0(\varepsilon_r' - j\varepsilon_r'')]}{Z_0 + 1/[j\omega C_0(\varepsilon_r' - j\varepsilon_r'')]},$$

(4.7)

whereupon the real and imaginary parts of the permittivity can be solved as

$$\varepsilon_r' = \frac{-2|\rho_L|\sin\phi}{\omega C_0 Z_0(1 + 2|\rho_L|\cos\phi + |\rho_L|^2)},$$

(4.8)

$$\varepsilon_r'' = \frac{1 - |\rho_L|^2}{\omega C_0 Z_0(1 + 2|\rho_L|\cos\phi + |\rho_L|^2)},$$

(4.9)

where ϕ is the phase angle of ρ_L. More accurate analysis methods also take into account C_f and G_0. [33]

4.3.2 Dielectric Measurement Results

The real and imaginary parts of the relative permittivity were measured for the glucose solution and for the CTC in a frequency range of 20 MHz - 5 GHz. Altogether, 21 measurements were conducted, as seen in Table 4.2. The glucose solution was measured with the concentration varying from 0 to 100 mmol/l and the temperature varying from 20 to 40 °C, which are normal values under operation [36]. The temperature was measured with a Fluke 52 K thermometer, whose measurement accuracy is ±1.1 °C [37].

The real and imaginary parts of the relative permittivity from measurements 6 to 10 (Table 4.2) are presented in Fig. 4.7. The loss tangent, calculated with Eq. (4.3), is presented in Fig. 4.8. A higher temperature is represented with a thicker line. As can be seen from Fig. 4.7, both the real and the imaginary part of the permittivity decrease as the temperature rises. This can be explained with the Debye relaxation model for liquids with polar molecules, which reads [38]

$$\varepsilon(\omega) = \varepsilon_\infty + \frac{\varepsilon_s - \varepsilon_\infty}{1 + j\omega\tau_D},$$

(4.10)

where $\varepsilon_s = 190.0 - 375T$ is the low-frequency permittivity, $\varepsilon_\infty = 4.9$ is the high-frequency permittivity, $\tau_D = \frac{1.99}{T}e^{2140/T} \times 10^{-12}$ is the relaxation time and T is the temperature in Kelvin. On frequencies below 5 GHz, the equation yields that both the real and the imaginary part of the permittivity decrease as the temperature rises. The loss tangent decreases in the same manner as the real and imaginary part of the permittivity, as shown in Fig. 4.8. The figures also show the frequency characteristics. Similar figures can be drawn for measurements 1-5 and 11-20, which likewise show the downward trend resulting from a temperature rise.

The permittivity measurements for the battery water with various concentrations of

Table 4.2: Performed permittivity measurements

	Material under test	Concentration [mmol]	Temperature [°C]
1.			20
2.			25
3.	Battery water (distilled water) (40 g)	0	30
4.			35
5.			40
6.			20
7.			25
8.	Battery water (40 g) + glucose (0.72 g)	10	30
9.			35
10.			40
11.			20
12.			25
13.	Battery water (40 g) + glucose (3.6 g)	50	30
14.			35
15.			40
16.			20
17.			25
18.	Battery water (40 g) + glucose (7.2 g)	100	30
19.			35
20.			40
21.	CTC	-	25

glucose are corresponding with earlier permittivity investigations [39–41]. A comparison between the measurement results and previous results [39] for battery water is presented in Table 4.3. It is noticed, that the measured permittivities are congruent with previous results. The measured permittivity for 0.1 GHz at 25 °C has a very small imaginary part (0.1) compared to the value presented in literature (0.4), but this difference is a result of inaccuracy in the measurements. Observing the measurement results (Figs. 4.7 to 4.12) and especially the uneven shape of the graph lines, it is obvious that there is some uncertainty in the measurements due to inaccuracy in the calibration.

Table 4.3: Difference between measured and previously obtained relative permittivity results for battery water.

Temperature [°C]	Frequency [GHz]	Measured Permittivity	Permittivity presented in [39]
25	0.1	$78.9 - j0.1$	$78.0 - j0.4$
25	3.0	$76.5 - j12.0$	$76.7 - j12.0$
35	0.3	$75.8 - j1.0$	$74.0 - j0.9$
35	3.0	$74.1 - j9.2$	$74.0 - j9.4$

The impact of increasing the concentration can be seen as a thickening line in Figs. 4.9 and 4.10, which present measurements 2, 7, 12 and 17. The temperature is constant (25 °C) and the concentration increases from 0 to 100 mmol/l. It can be seen that the loss tangent increases with increasing concentration. This is natural, since the glucose molecules, which are larger than water molecules, have a smaller real part and larger imaginary part of the permittivity compared to water (on the investigated frequency range) [42].

As can be seen by observing Eqs. (3.43) and (4.5), higher permittivity lowers the characteristic impedance and increases the wavelength. Eqs. (3.45) and (4.3) show the influence of the growing loss tangent on the dielectric attenuation, which can be seen in Fig 4.8.

The permittivity of the CTC was measured in order to determine whether the material is a dielectric or a conductor. Although permittivity measurements do not directly give accurate conductivity results, they may provide an indication on the conductivity of the material. As seen in Figs. 4.11 and 4.12, the permittivity was high, which suggests that the material is fairly conductive. This assumption follows from the fact that the metallic short applied for calibrating the probe gives the highest possible relative permittivity (10000) at all frequencies. The conductivity of the CTC was also tested with a volt-ohm meter (DC), whereupon good conductivity was detected. The conductivity on higher frequencies could not be measured directly, but it was assumed that the CTC layer is a decent conductor because carbon is a good electric conductor. It must nonetheless be noted, that the measurement results for the CTC are to be treated with great reservation, because the relative permittivity is not between 2.5 and 80 (Sec. 4.3.1), which was the requirement in order to gain reliable measurement results. Using Eq. (4.6) at 2.5 GHz, we get $\sigma \approx 139$ S/m. The conductivity value indicates that the CTC resembles a semiconductor. The permittivity of the CTC can also be shown with logarithmic axes, in which case a straight line is obtained. This indicates, that the conductivity of the material is nearly constant.

The fuel cell dielectric can be approximated using the effective relative permittivity, presented in Sec. 3.5, which can be calculated with (3.52). The permittivity is shown in Fig. 4.13 and the loss tangent in Fig. 4.14. The characteristics of the glucose-battery water solution varied widely depending on the concentration and temperature, as shown in Figs. 4.7 to 4.10, and in this calculation the fuel solution is portrayed by measurement 13 in Table 4.2, because the concentration and temperature values are approximately average values considering the range of variation.

The wavelength for the effective dielectric can be calculated with (4.5) to be approximately 12 to 14 times shorter than in vacuum. At 1 GHz, $\lambda \approx 20$ mm.
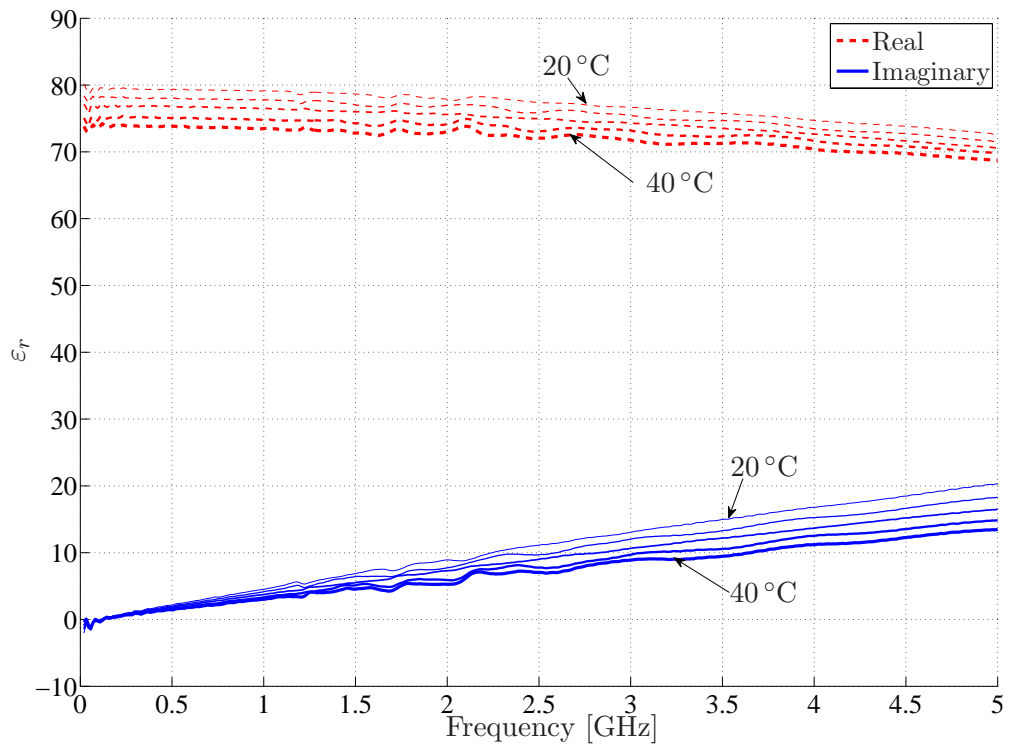
Fig. 4.7: Real and imaginary parts of the relative permittivity for a glucose solution with 10 mmol/l concentration when temperature varies from 20 to 40 °C in 5 °C steps. The thicker line represents higher temperature.
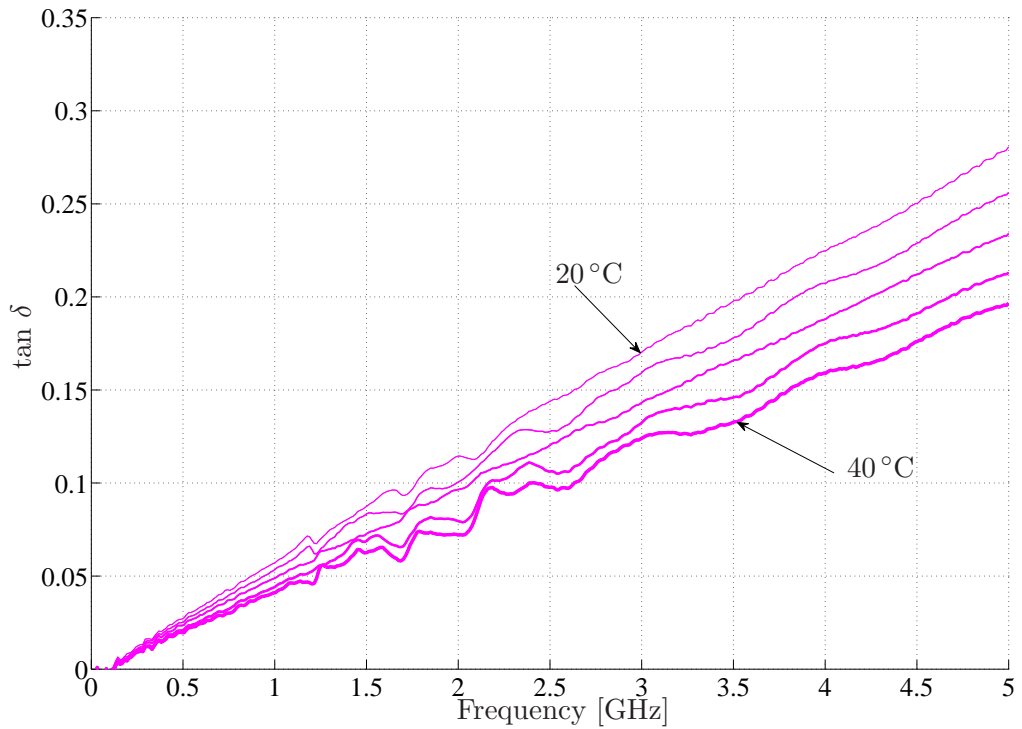

Fig. 4.8: Loss tangent for the glucose with 10 mmol/l concentration when temperature varies from 20 to 40 °C in 5 °C steps. The thicker line represents higher temperature.
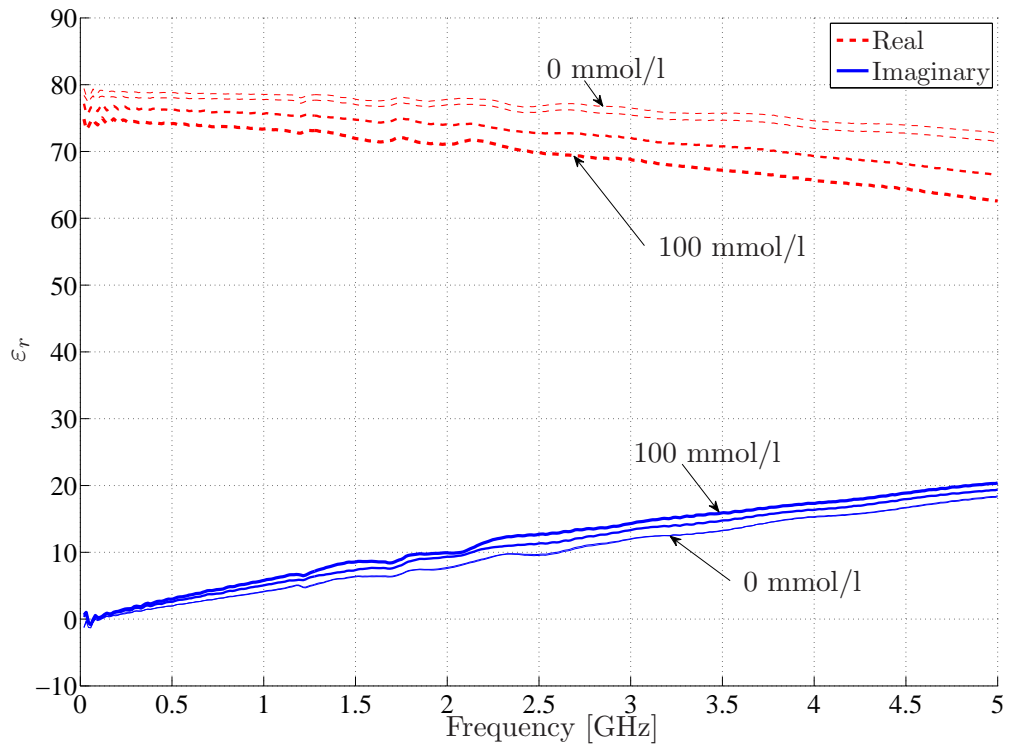
Fig. 4.9: Real and imaginary parts of the relative permittivity for a glucose solution when the concentration varies from 0 to 100 mmol/l. The temperature is constant at 25 °C. The thicker line represents higher concentration.
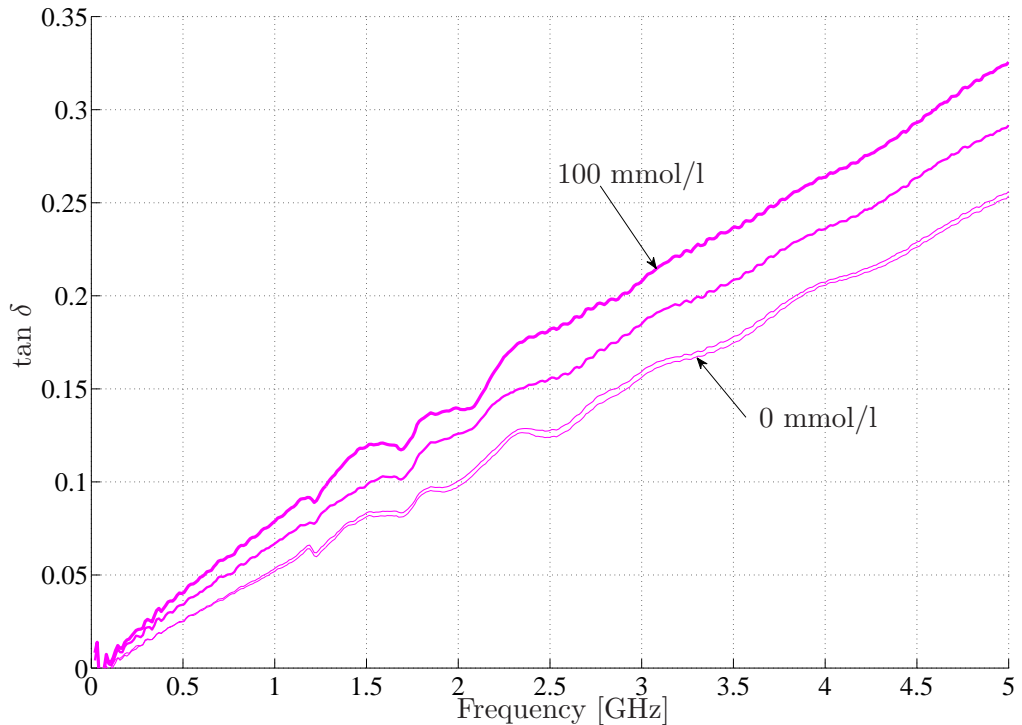

Fig. 4.10: Loss tangent for the glucose solution when the concentration varies from 0 to 100 mmol/l. The temperature is constant at 25 °C. The thicker line represents higher concentration.
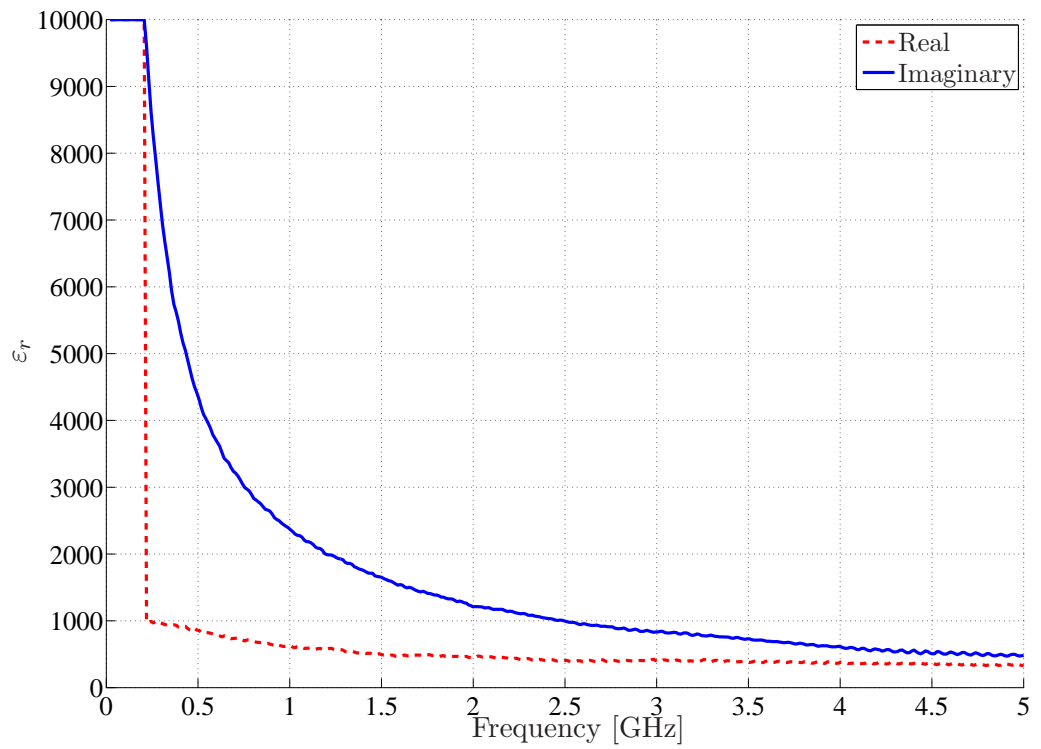
Fig. 4.11: Real and imaginary parts of the relative permittivity for the CTC layer at room temperature.
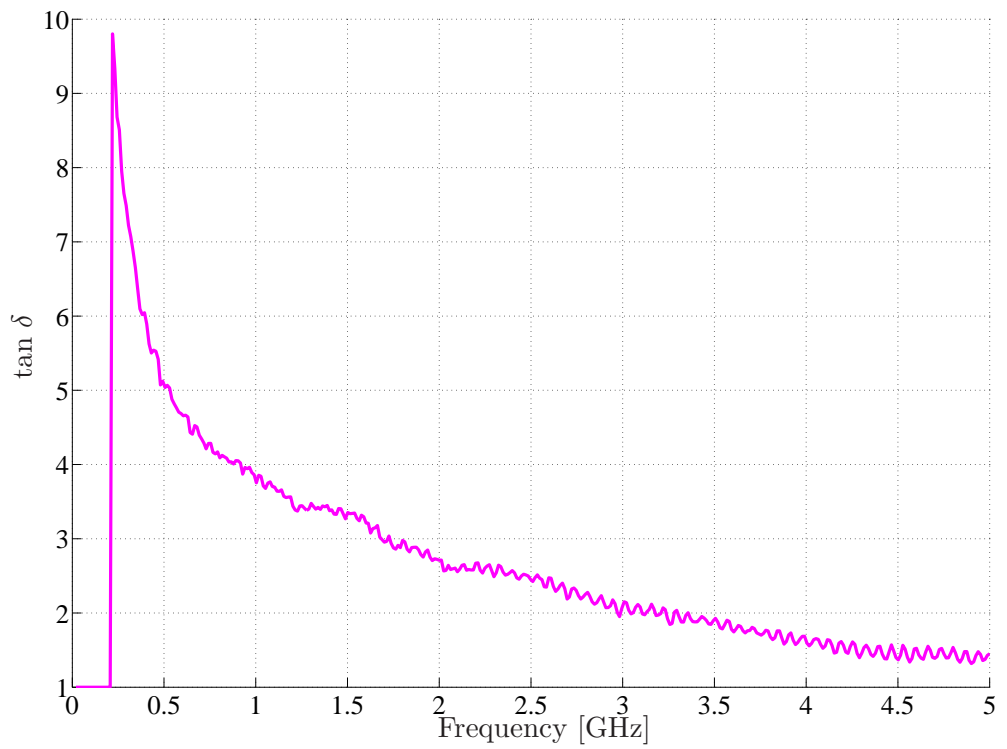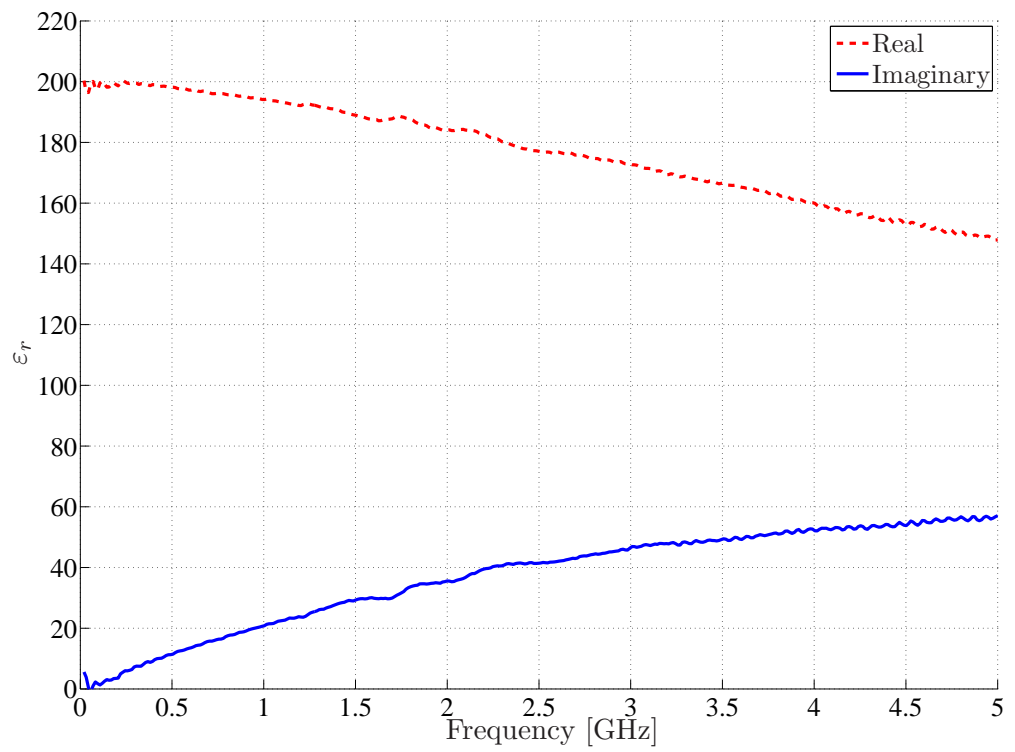

Fig. 4.12: Loss tangent for the CTC layer.

Fig. 4.13: Real and imaginary parts of the effective relative permittivity for the combined dielectric.
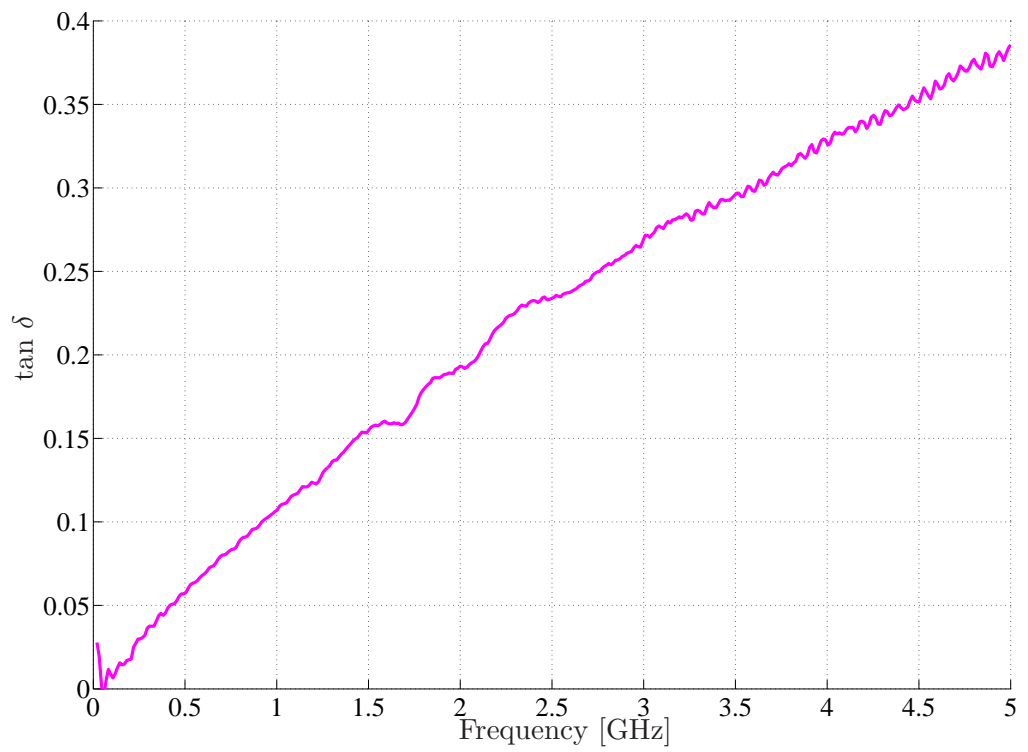

Fig. 4.14: Effective loss tangent for the combined dielectric.

CHAPTER 5

IMPLEMENTATION OF THE SIGNAL FEED

In order to generate a time-harmonic electromagnetic field into the fuel cell, a signal generator must be connected to the fuel cell. A means of doing this is to use a matching part. Since the size difference between any signal generator feed cable and the fuel cell is remarkable, the matching part has to be tapered. Additionally, the matching part could reasonably be coaxial, due to the coaxial output of the used signal generator and the coaxial structure of the fuel cell. The frequency under focus ranges from 50 MHz to 5 GHz.

This chapter presents the feeding of the signal and the related matching difficulties. Different tapering methods, particularly methods concerning coaxial cables, are compared with the assistance of calculus and simulation. Also attenuation of the fuel cell dielectric and alternative signal feed structures are discussed.

5.1 Impedance Matching

Until now in this study, waveguides have been assumed to be homogeneous and infinite, in which case terminations, size variations or other discontinuities of the cable have not been of interest. However, discontinuities in a cable cause reflections, which prevent a part of the signal power from penetrating through the discontinuity and instead reflects towards the source of the signal [21]. A difference in the characteristic impedance causes a reflection when connecting two coaxial cables [20, 21].

5.1.1 Reflection Coefficient

As discussed in Sec. 3.4.3, a coaxial cable has a specific characteristic impedance Z_0, calculated with (3.43), depending on the diameters of the conductors and the electrical properties of the dielectric. If a cable with the characteristic impedance Z_0 (cable 1) is connected to a cable with the impedance Z_L (cable 2) as in Fig. 5.1, the voltage reflection coefficient can be calculated with [20, 21]:

$$\rho_L = \frac{V^+}{V^-} = \frac{Z_L - Z_0}{Z_L + Z_0},\tag{5.1}$$

where V^+ is the amplitude of the wave propagating in the z direction in cable 1 and V^- is the amplitude of the reflected wave propagating in the $-z$ direction. The voltage transmission coefficient is [21]

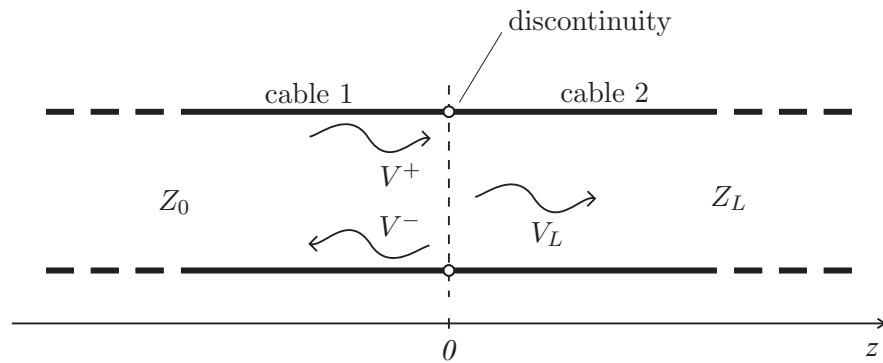$$\tau_L = 1 + \rho_L = \frac{2Z_L}{Z_L + Z_0}.\tag{5.2}$$

Fig. 5.1: Wave propagation and reflection in waveguides.

The time-average power flowing through the discontinuity is [20]

$$P_{av} = \frac{1}{2}\frac{|V^+|^2}{Z_0}(1 - |\rho_L|^2).\tag{5.3}$$

The maximum power is delivered to the second cable when the reflection coefficient $\rho_L = 0$ and no power delivered when $\rho_L = 1$, which means that all power is reflected at the discontinuity [20, 21]. When $\rho_L = 0$, cable 2 is said to be *matched* to cable 1, and in other cases the connection is *mismatched*. When the other cable is mismatched, not all of the available power from cable 1 is delivered to cable 2. This loss is referred to as *return loss* (*RL*), and is defined as [20, 21]:

$$RL = -10\log|\rho_L|^2 \text{ dB},\tag{5.4}$$

which means that a matched case has an infinite return loss and a total reflection ($\rho_L = 1$)

has a return loss of 0 dB [20]. Alternatively, this loss caused by mismatching can be expressed with the ratio of the power received through the discontinuity and the power transmitted into the line [43] as *insertion loss* (IL), and can be written as [21]

$$IL = -10 \log \frac{1}{1 - |\rho_L|^2} \text{ dB.} \tag{5.5}$$

5.1.2 Standing Waves

In a matched lossless cable, the amplitude of the voltage remains unchanged throughout the cable, but in mismatched cases reflections cause waves propagating in the opposite direction. This leads to standing waves where the amplitude of the voltage in the cable is not constant [20]. The maximum voltage V_{max} is acquired when the propagating and reflected waves are in the same phase and their voltages are combined. Thus, [20, 21]

$$V_{max} = |V^+| + |V^-| = |V^+|(1 + |\rho_L|). \tag{5.6}$$

The minimum voltage V_{min} is by the same token located where the incoming and reflected wave have opposite phase and the total voltage is the difference between the voltage amplitudes, written as [20, 21]

$$V_{min} = |V^+| - |V^-| = |V^+|(1 - |\rho_L|). \tag{5.7}$$

The standing wave ratio (SWR) is defined as the ratio between V_{max} and V_{min} [20, 21]:

$$SWR = \frac{V_{max}}{V_{min}} = \frac{(1 + |\rho_L|)}{(1 - |\rho_L|)}, \tag{5.8}$$

which is a measure of mismatch since as the reflection coefficient increases, so does the SWR. In a matched situation the $SWR = 1$ and if $\rho_L = 1$, SWR is infinite [20, 21].

5.2 Electromagnetic Characteristics of the Fuel Cell

The permittivity measurements, presented in Sec. 4.3.2, assert that the permittivity for the fuel solution and the CTC is not constant, but depends on the frequency. Furthermore, the permittivity of the glucose solution also depends on the concentration and the temperature. Thus, the characteristic impedance inside the fuel cell is not static.

Using Eq. (3.51), the characteristic impedance Z_0 can be calculated for every measurement presented in Table 4.2. The impedance is found to vary between 0.52 and 0.61 Ω inside the fuel cell, if the conductivity of the CTC is assumed to be low according to the conductivity calculus performed in Sec. 4.3.2. The impedance can also be calculated

with (3.43), using the effective permittivity (Sec. 3.5), which yields the same result. If the conductivity of the CTC is assumed very high, the dielectric is formed only out of the glucose solution layer, whereupon the thickness of the dielectric is smaller. Now, the characteristic impedance is even lower, varying between 0.25 and 0.35 Ω.

At the beginning of the fuel cell, as the first material into which the electromagnetic field penetrates, is the PSU plug as seen in Fig. 4.2. The real part of the relative permittivity varies approximately between 3.0 and 3.5 [44,45], and is also slightly frequency dependent. The PSU used in the fuel cell has an approximate permittivity of 3.2 and a loss tangent of 0.006 [46]. With this dielectric and regarding the dimensions, the characteristic impedance at the beginning of the fuel cell can be calculated to be $Z_0 = 8.4$ Ω. In the simulations this characteristic impedance is used as the load impedance, Z_L, to which the matching part is tapered. The decision to taper the matching part to this impedance was made because at this stage the structure of the fuel cell and the length of the plastic plug were unknown. The characteristic impedance of the signal generator output is $Z_0 = 50$ Ω.

In Sec. 3.4.3 the condition for preventing the existence of lossy TE and TM modes is presented with (3.46). For the fuel cell the equation is satisfied only below approximately 360 MHz, when the real part of the relative permittivity is approximated as 75.

5.3 Coaxial Cable Tapering

As discussed in Sec. 5.1, impedance mismatch often occurs when connecting transmission lines. The reflections can be decreased by using a tapered matching part between the lines [20]. A tapered waveguide is "A waveguide in which a physical or electrical characteristic varies continuously with distance along the axis of the guide" [47], and literature presents many methods for tapering a transmission line from a smaller impedance to a larger impedance [20]. The manufacturing equipment constricts the length of the taper, as well as the shape, which has to be stepped (Sec. 5.4.1).
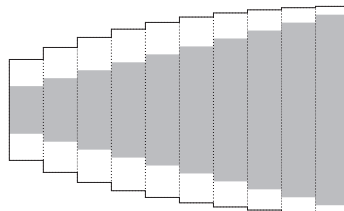

Fig. 5.2: Tapering of a coaxial cable with 10 steps; the inner conductor is shown as grey.

Many methods can be considered for tapering any transmission line from a smaller impedance Z_0 to a larger impedance Z_L stepwise (see Fig. 5.2). To keep the reflection

coefficient ρ_L constant between every step of the tapering is one possible alternative. Another method for doing this would be to keep the impedance change constant from one step to another. Also, changing the diameter of both the inner and the outer conductor in constant steps, is one alternative.

Literature presents the Klopfenstein taper as the optimum method for a given taper length L, compared to the exponential and the triangular tapers [20]. The triangular taper was not taken into account in the taper comparison, because according to [20], this taper is the slowest to reach the desired reflection coefficient, thus having a larger reflection coefficient on lower frequencies, which potentially form the specific area of interest. A multisection quarter-wave transformer can also be used to change the characteristic impedance of a coaxial cable [21], but in this specific application the implementation is impossible, because the length of the matching part is restricted.

5.3.1 Constant Reflection Coefficient

As mentioned in Sec. 5.1, the reflection coefficient ρ_L between two steps with the characteristic impedances Z_1 and Z_2 is

$$\rho_L = \frac{Z_2 - Z_1}{Z_2 + Z_1}.$$

If the reflection coefficient is constant at ρ, we obtain the impedance of the first and second step of the taper as

$$Z_1 = Z_0 \frac{1 + \rho}{1 - \rho},$$

$$Z_2 = Z_1 \frac{1 + \rho}{1 - \rho} = Z_0 \left(\frac{1 + \rho}{1 - \rho}\right)^2,$$

where Z_0 is the initial impedance. Finally, we can set up an equation for the end impedance Z_L, when the number of steps is n, as

$$Z_L = Z_n \frac{1 + \rho}{1 - \rho} = Z_0 \left(\frac{1 + \rho}{1 - \rho}\right)^{n+1}. \tag{5.9}$$

Now we can calculate the reflection coefficient

$$\rho = \frac{\left(\frac{Z_L}{Z_0}\right)^{\frac{1}{n+1}} - 1}{\left(\frac{Z_L}{Z_0}\right)^{\frac{1}{n+1}} + 1}. \tag{5.10}$$

5.3.2 Constant Impedance Change

If the characteristic impedance between the steps changes constantly, the calculus is done simply by calculating the step size when the initial impedance Z_0, the end impedance Z_L and the number of steps n are known. The step size Z_{step} can be calculated with

$$Z_{step} = \left| \frac{Z_L - Z_0}{n + 1} \right|. \tag{5.11}$$

5.3.3 Constant Diameter Change

Both the inner and outer diameters of the coaxial taper can be changed with constant steps. In this case the characteristic impedance for a single step can be evaluated with (3.43). This is the simplest method and requires minimum calculation in order to simulate or manufacture the taper.

5.3.4 Exponential Taper

According to [20], the exponential taper should be fast to reach a desired reflection coefficient. The characteristic impedance along the taper is calculated with [20]

$$Z(z) = Z_0 e^{az}, \tag{5.12}$$

where $0 \leq z \leq L$. In order to have $Z(0) = Z_0$ at the beginning of the taper and $Z(L) = Z_L = Z_0 e^{aL}$ at the end, the constant a in (5.12) can be determined as [20]

$$a = \frac{1}{L} \ln \left(\frac{Z_L}{Z_0} \right). \tag{5.13}$$

5.3.5 Klopfenstein Taper

For a given taper length, the Klopfenstein impedance taper has been considered to be optimum when a small reflection coefficient is required over the passband [20, 48]. The Klopfenstein taper is essentially an infinitely stepped Chebyshev transformer and also analogous to the Taylor distribution of antenna array theory [20].

The design of the taper begins by choosing a maximum passband ripple ρ_m and calculating the zero frequency reflection coefficient ρ_0 with (5.1), when the length of the taper L, the initial impedance Z_0 and the end impedance Z_L are known. This allows

the calculation of A, which is obtained from the equation

$$\cosh A = \frac{\rho_0}{\rho_m}. \tag{5.14}$$

The logarithm of the characteristic impedance Z along the Klopfenstein taper is calculated with

$$\ln Z(z) = \frac{1}{2} \ln Z_0 Z_L + \frac{\rho_0}{\cosh A} A^2 \phi(2z/L - 1, A), \tag{5.15}$$

where $0 \leq z \leq L$ and the function $\phi(x, A)$ is defined as

$$\phi(x, A) = -\phi(-x, A) = \int_0^x \frac{I_1(A\sqrt{1-y^2})}{A\sqrt{1-y^2}} dy, \tag{5.16}$$

for which $|x| \leq 1$ and $I_1(x)$ is the modified Bessel function. The function in (5.16) takes the following special values:

$$\phi(0, A) = 0,$$

$$\phi(x, 0) = \frac{x}{2},$$

$$\phi(1, A) = \frac{\cosh A - 1}{A^2},$$

but is otherwise calculated numerically. In this work, ρ_m has been chosen to be 0.1. It is noted, that if ρ_0 is miscalculated, also ρ_m is changed. [20]

5.3.6 Simulations

In this work, all simulations have been performed using the Ansoft HFSS (High Frequency Structure Simulator) electromagnetic field simulation tool, version 11.2.0. The program is based on the finite element method (FEM) in order to compute the electromagnetic behavior of components in the frequency domain [49]. The simulated reflection coefficient and gain for the matching part are presented in Fig. 5.9.

5.3.7 Taper Comparison

The taper methods mentioned previously were simulated in order to find the matching part with the highest gain. The gain is simulated for the constant reflection coefficient, constant impedance change, constant diameter change, exponential and Klopfenstein tapers (see Fig. 5.3). The length $L = 60$ mm and the amount of steps was $n = 10$. It is seen that the Klopfenstein taper has the lowest attenuation at frequencies below 2 GHz, compared to the other tapering methods.
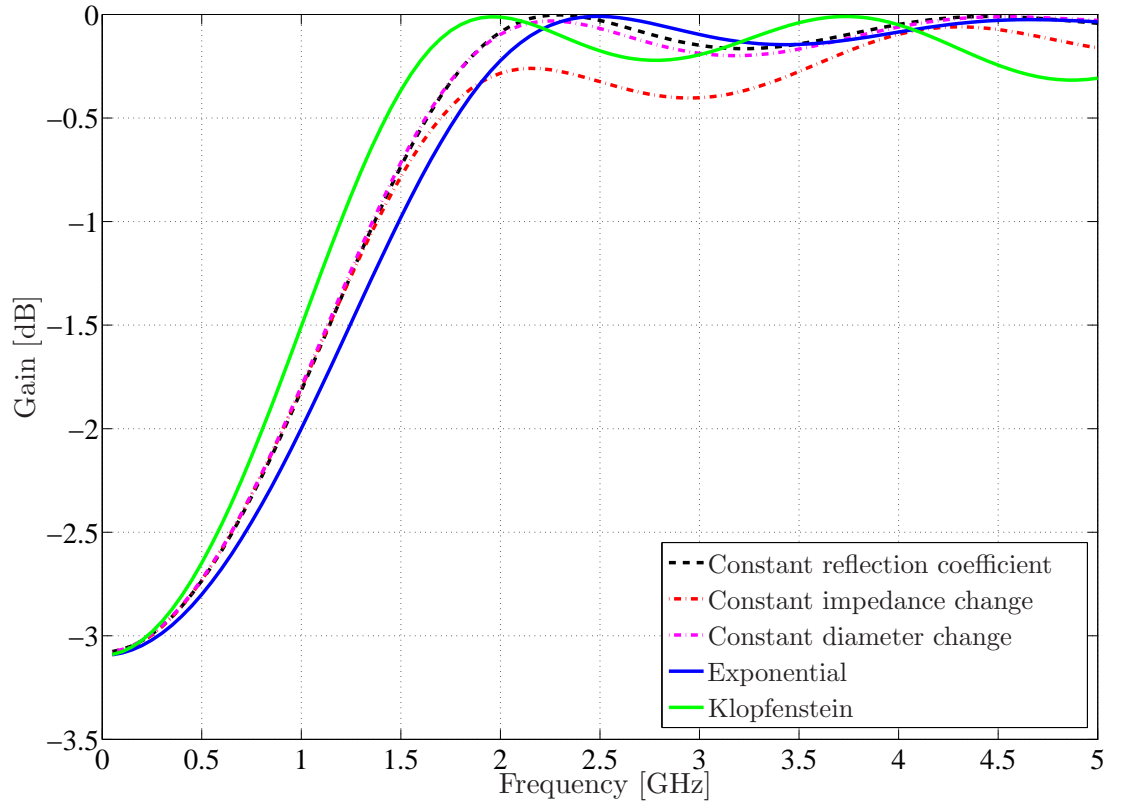
Fig. 5.3: Comparison of tapering methods. $L = 60$ mm, $n = 10$, $Z_0 = 50$ Ω and $Z_L = 8.4$ Ω.

Influence of the Length

In general, a longer taper reduces the attenuation. This is seen by simulating a Klopfenstein taper with different length and comparing the results presented in Fig. 5.4. The length in the simulation varied from 30 to 155 mm.

Influence of the Number of Steps

Intuitively it would be assumed that a greater number of steps in the taper enhances the penetration through the matching part, as the shape of the taper increasingly starts to resemble a perfect cone. Simulations, however, suggest the opposite, as seen in Fig. 5.5. At lower frequencies, the gain is higher with only 5 steps in the taper compared to a larger amount of steps.

5.3.8   Tapering to Different Parts of the Fuel Cell

The easiest approach to the tapering problem is to ignore the structure of the fuel cell and taper the signal generator output to the end of the fuel cell, which in this case is
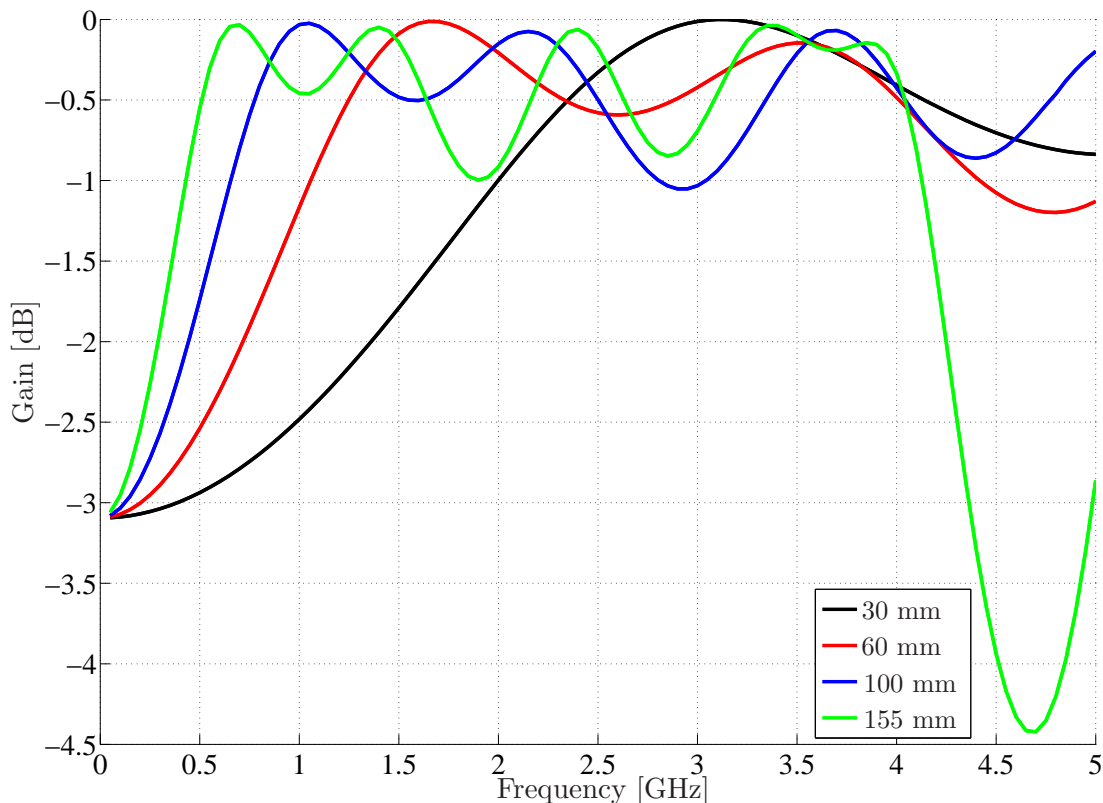
Fig. 5.4: Influence of the length on the gain of the matching part. $n = 5$, $Z_0 = 50$ Ω and $Z_L = 8.4$ Ω. Klopfenstein is the used tapering method.

the polysulfone plastic, as mentioned in Sec. 5.2, with a characteristic impedance of 8.4 Ω. On the other hand the tapering could be done directly to the actual substance of the fuel cell; the solution consisting of glucose and battery water. Thus, the polysulfone plug would be considered electrically short, whose effect in the propagation is small. Here, the characteristic impedance is, as calculated in Sec 5.2, approximately 0.6 Ω when the CTC layer is treated as a dielectric.

Hence, the taper can be designed from 50 to 8.4 or 0.6 Ω. These two approaches are compared with each other with simulations, where the transmission through the matching part and the polysulfone is examined. The taper to 8.4 Ω is the 5-step Klopfenstein taper that is used in the previous section. As the taper to 0.6 Ω, Klopfenstein could not be used, because it would have required numerous steps (> 20) in order to be manufacturable (see Sec. 5.4.1). Thereby, a 7-step taper using the constant impedance change-method was used instead. This was the only method, which could be manufactured with under 15 steps without short-circuiting the inner and outer conductor. The comparison is presented in Fig. 5.6, which shows the attenuation from the end of the signal generator cable to the beginning of the operational (liquid) part of the fuel cell. It can be seen that both approaches have their advantages. Below 1.6 GHz, tapering to 8.4 Ω is more profitable, and vice versa on frequencies above 1.6 GHz.
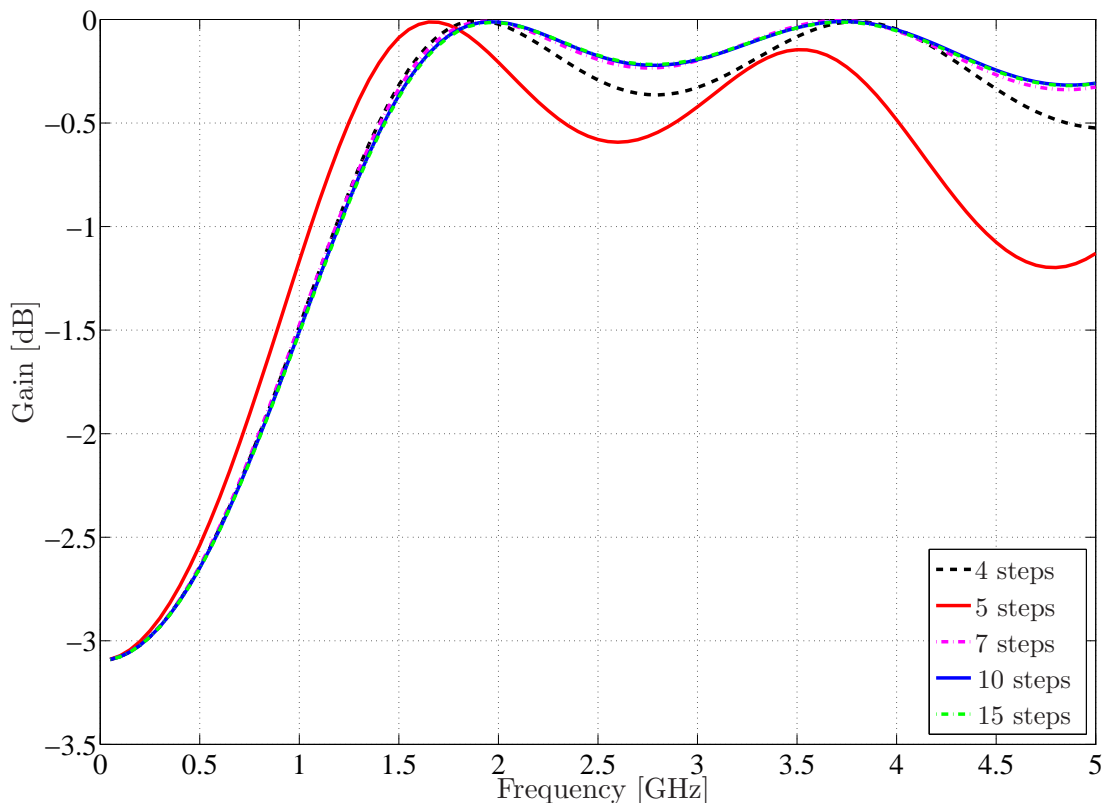
Fig. 5.5: Influence of the number of steps in the taper on the gain of the matching part. $L = 60$ mm, $Z_0 = 50\ \Omega$ and $Z_L = 8.4\ \Omega$. Klopfenstein is the used tapering method.

5.4 Prototype of the Matching Part

5.4.1 Manufacturing Constraints

The machining equipment at the Department of Radio Science and Engineering constricts the size and shape of the matching part. Firstly, the length of the matching part is limited to 60 mm due to the length of the drill bits. Secondly, the shape of the matching part cannot be formed into a cone, but the thickness has to be changed gradually in steps (Fig. 5.2). Last, air must be used as insulator, because machining dielectric material into perfect shape would be problematic. Brass is the material used for machining the matching part.

5.4.2 First Steps

Before building the matching part, a few simulations were conducted in order to clarify how the tapering could be realized for this application. In particular, a high gain at a wide frequency range was desired. The broad frequency band is required, since it
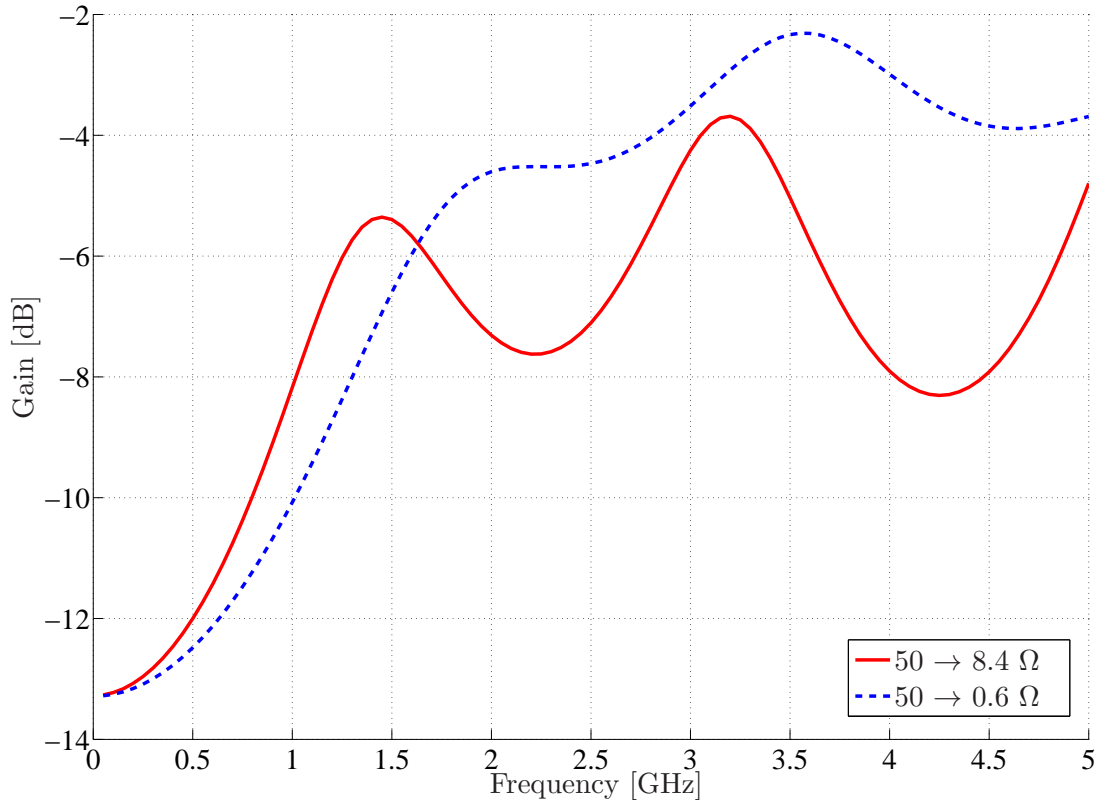
Fig. 5.6: Difference in the gain when designing the tapering to different parts of the fuel cell.

is not known whether a specific frequency or threshold frequency exists, at which the electromagnetic field enhances the operation of the fuel cell the most. The structure of the matching part is similar to the simulation model in Fig. 5.7.

In the design and manufacturing process, the most important matter regarding the matching part was to ensure knowledge of the reflection and transmission qualities. The first prototype was done early in order to be able to initiate the measurements as soon as possible. Also, it was done in the belief that a better, more optimized matching part would be constructed later if needed. Because of this, it was accepted that the first prototype was only able to transmit power at a required level in order to investigate the influence of the electromagnetic field, not to be perfectly optimized for the task.

The first matching part was made out of brass according to the first simulation results (Fig. 5.8), because it was important to have a working method for feeding the fuel cell. The tapering was done with constant diameter change, after this was found to be the least attenuating taper among the methods tested at that time (constant reflection coefficient and constant characteristic impedance change were the other methods). At the time of making the decision on the tapering method, the Klopfenstein method was not yet known. The same holds true for the knowledge of the precise fuel cell structure. Due to this, the matching was done to the end of the fuel cell (the PSU plug, with $Z_0 = 8.4 \ \Omega$)
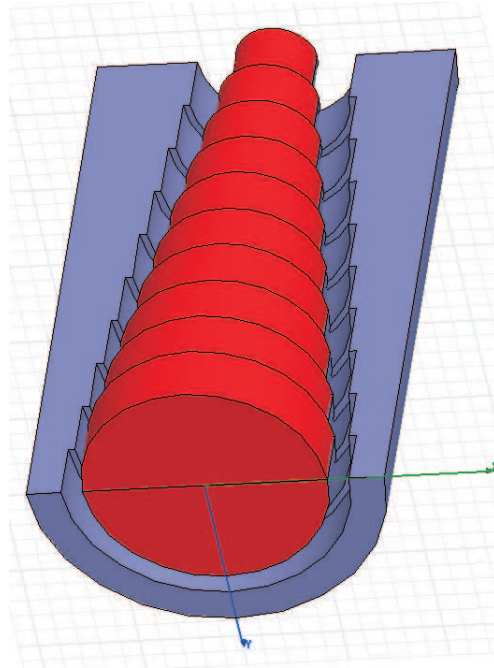
Fig. 5.7: HFSS simulation model for the matching part.

and not to the inside (the fuel solution, $Z_0 \approx 0.6\ \Omega$). The simulated reflection coefficient ρ_L and gain for the matching part are presented in Fig. 5.9.

<div align="center">a)   b)</div>
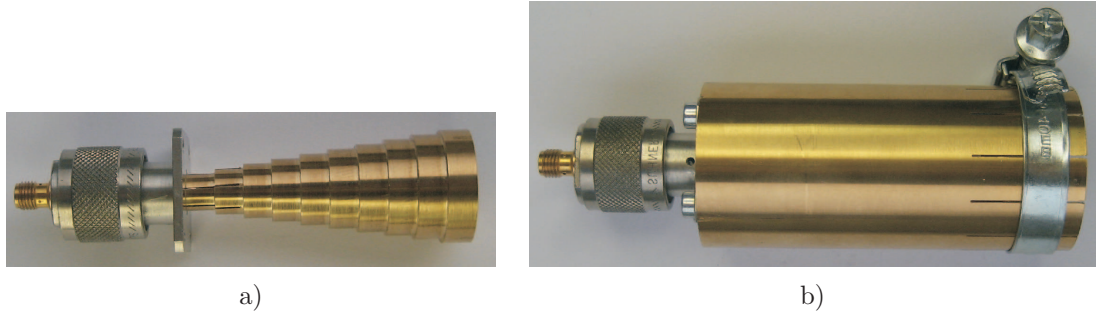
Fig. 5.8: Inner a) and outer b) conductor of the matching part, connected to a 50 Ω SMA-N type connector.

5.4.3 Measurements

The simple matching part presented in Figs. 5.7 and 5.8 cannot be measured entirely, because no adapters are suitable for connections to the wider side of the matching part. This questions the simulation results which were obtained in the previous section, see Fig. 5.9.

One solution is to connect two matching parts in series according to Figs. 5.10 and 5.11. This structure can be measured and thus compared with the simulation results. These

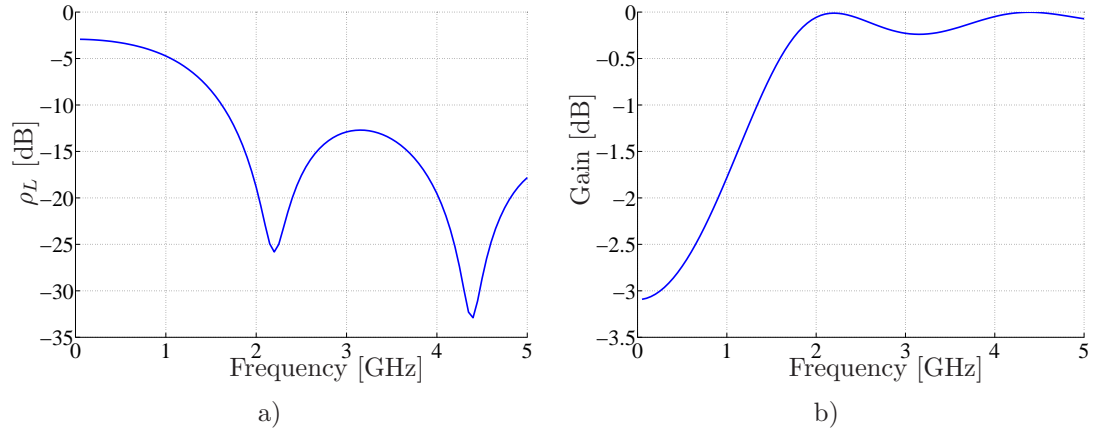a)   b)

Fig. 5.9: Reflection coefficient and gain for the first matching part prototype. Z_0=50 Ω and Z_L=8.4 Ω.

results are presented in Fig. 5.12, and it can be seen that at frequencies below 2 GHz, the measured response is very similar to the simulated response. Hence, it can be assumed that the simulations are valid also for the simple matching part in this frequency range. As will be discussed in Sec. 5.5, higher frequencies are assumed to be of lesser interest.
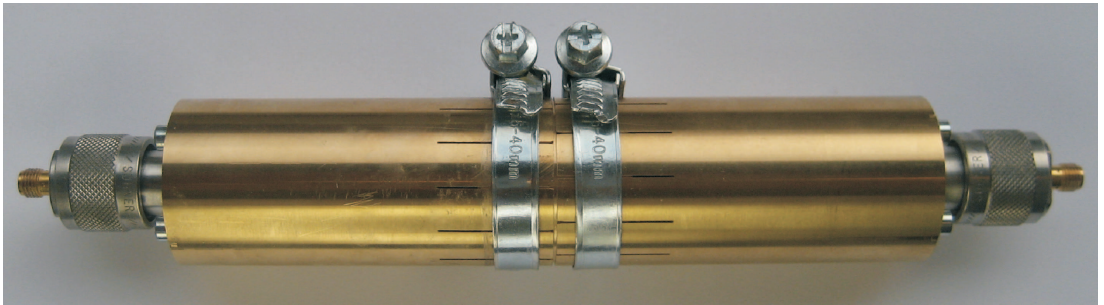

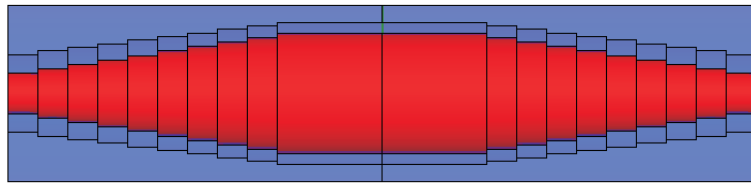Fig. 5.10: Photograph of the connected matching parts.

Fig. 5.11: Simulation model for two matching parts in series.

5.5 Influence of Attenuation Inside the Fuel Cell

In Sec. 4.3.2, the dielectric measurement results for the dielectric materials of the fuel cell, the fuel solution and the CTC, are presented. As can be seen from Fig. 4.13, the
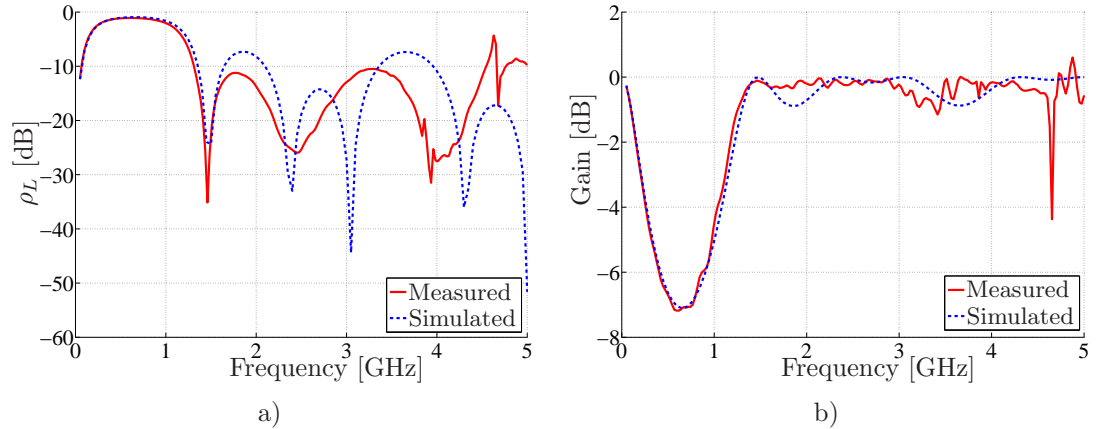
Fig. 5.12: Simulated and measured reflection coefficient and gain for the double matching part.

effective relative permittivity is high, which according to Eqs. (4.3) and (3.45) leads to a high attenuation of the electric field.

The losses in dielectric matter occur partly due to the small conductivity the unideal dielectric possesses, in which the electric field produces a small electric current according to (3.5), and the electric power is converted to heat [50–52]. The heat generated can be calculated with [51,52]

$$W_{heat} = \frac{E^2 f \varepsilon_r \tan \delta}{1.8 \cdot 10^{12}}. \tag{5.17}$$

Thus, the energy is preserved according to the first law of thermodynamics, but converted to heat [5].

The calculated and simulated attenuation L_c for the fuel cell is presented in Fig. 5.13. The theoretical estimation of the attenuation, is calculated with [20]

$$L_c \text{ [dB]} = -20 \log_{10} e^{-\alpha l}, \tag{5.18}$$

where α is calculated with (3.45) and l is the length of the operational part of the fuel cell (220 mm). In Eq. (3.45) it is assumed that $\tan \delta \ll 1$, which evidently is not the case for the CTC, as seen from Fig. 4.12. However, this equation is used because it is the best approximation available. For a more accurate solution, α can be obtained from (4.4), where there is no restrictions for $\tan \delta$. It is nevertheless evident that the attenuation is so strong, that the electromagnetic field exists only at the beginning of the fuel cell, due to the large losses of the dielectric. The large attenuation gives reason to believe, that frequencies above 1 GHz should not be used, because here the attenuation exceeds 30 dB. The glucose solution and the CTC layer have not been modeled separately in the simulation model, but the effective permittivity (Fig. 4.13) has been used to describe the two dielectric layers.

The attenuation per centimeter in dB at different frequencies is presented in Table 5.1
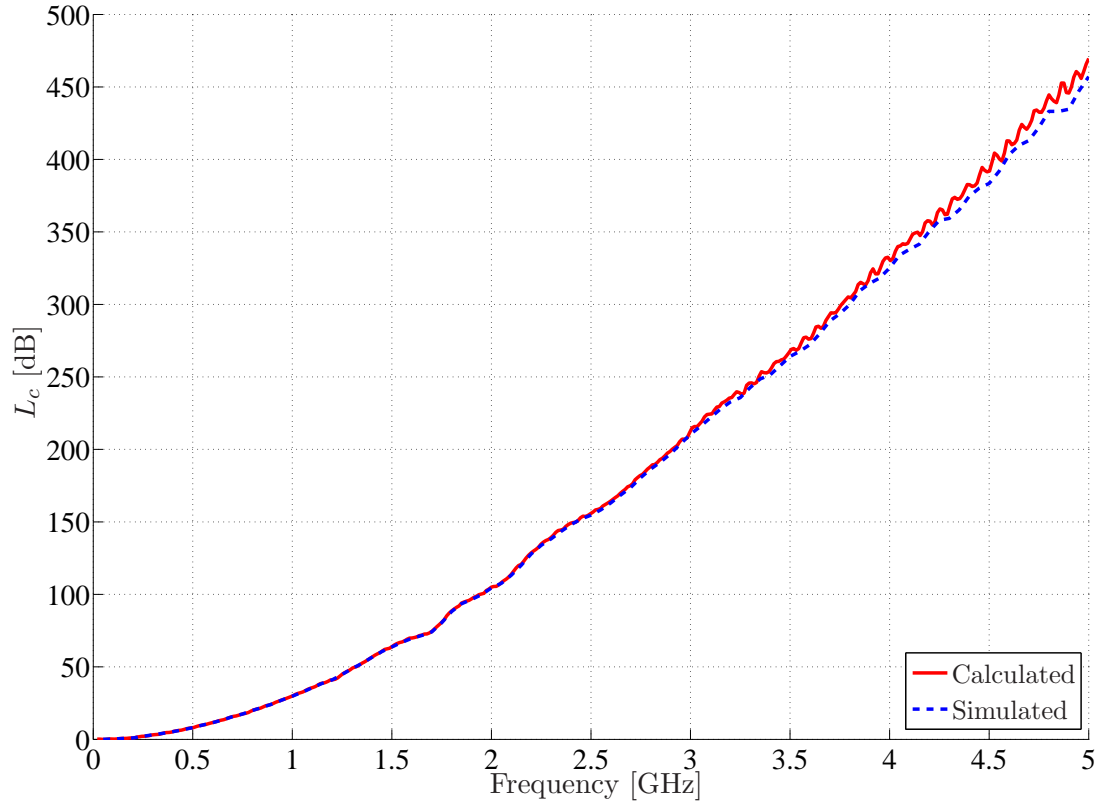
Fig. 5.13: Calculated and simulated attenuation of the fuel cell.

Table 5.1: Calculated attenuation of the fuel cell on different frequencies.

Frequency [GHz]	0.1	1.0	2.0	3.0	4.0	5.0
Attenuation [dB/cm]	0.01	1.36	4.77	9.67	15.04	21.35

Previously in Sec. 4.3.2, it was assumed that the conductivity of the CTC is not exceptionally high. However, if it would be very high (close to a perfect electric conductor), the electromagnetic field inside the fuel cell exists only in the glucose, whereupon the attenuation is approximately according to Fig 5.14. This assumption is made because no accurate conductivity measurement has been conducted for the CTC. Here, the fuel solution is again approximated by measurement 13 in Table 4.2. By comparing Figs. 5.13 and 5.14, it is noted that the attenuation in the glucose solution and in the CTC are of the same order of magnitude.

5.6 Other Methods for Signal Feeding

The electromagnetic field inside the fuel cell attenuates strongly, as seen from Fig. 5.13, which means that the field at the other end is non-existent and the effect of the field
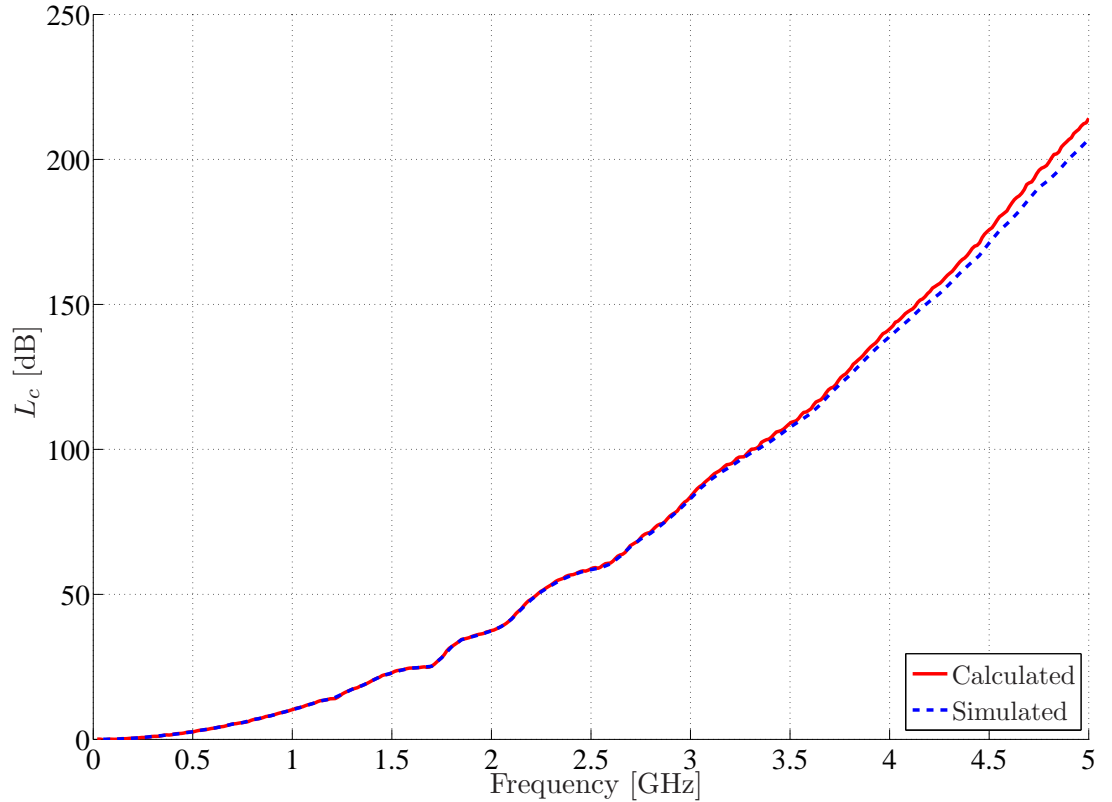
Fig. 5.14: Calculated and simulated attenuation of the fuel cell dielectric when the conductivity of the CTC layer is assumed very high.

is concentrated only on the forepart of the fuel cell. This problem could be diminished by circulating the fuel, but then the matching part could not be used and other feeding methods would have to be considered. Among these are the probe feed and the radiating cable.

5.6.1 Probe Feed

One possible feed structure is presented in Fig. 5.15. This coaxial probe, which is very narrow-band, could be attached to the lateral area of the fuel cell, enabling both ends of the fuel cell to be used for circulating the fuel. Circulation of fuel, as discussed in Sec. 2.2, improves the operation of the fuel cell by removing heat and exchanging the fuel.

Multiple probes could also be used to make the total field inside the fuel cell more uniform. When the specific operating frequency is known, the probe feed needs not to be broadband and the matching becomes much simpler.
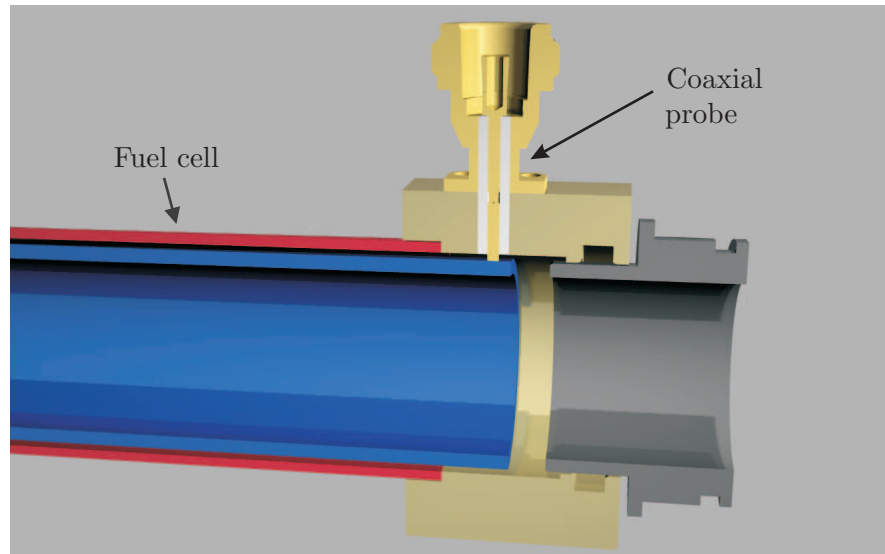
Fig. 5.15: Coaxial probe feed.

5.6.2 Radiating Coaxial Cable

Radiating or leaky coaxial cables (Fig. 5.16), are coaxial cables with slots in the outer conductor in order to allow the electromagnetic field to penetrate out of the cable [53]. They have been used in for instance railway tunnels and coal mines [53].
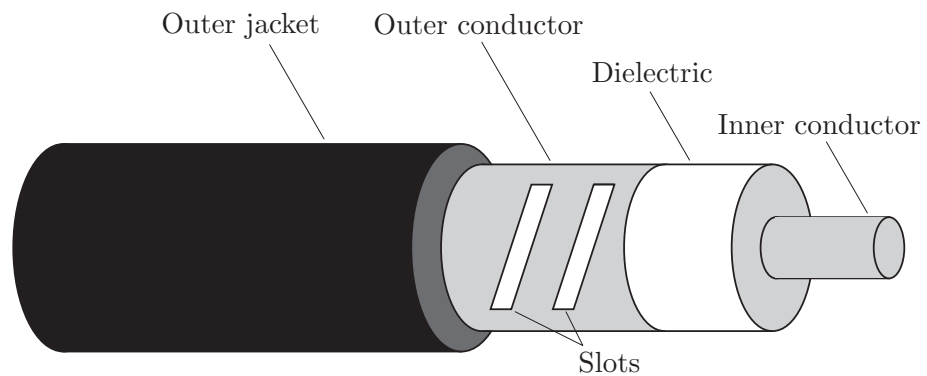
Fig. 5.16: Leaky coaxial cable [53].

A leaky coaxial cable could be connected side by side with the fuel cell, and if slots were made also to the outer conductor of the fuel cell, the leaky coaxial cable could feed an electromagnetic field directly into the fuel cell. With multiple slots, the field inside the fuel cell could be very uniform, and the slots could be optimized when the operation frequency would be known [53]. The feed of the radiating cable would also allow circulation of fuel.

CHAPTER 6

OUTPUT POWER MEASUREMENTS

This chapter describes the measurements performed to investigate the influence of a time-harmonic electromagnetic field on the output power of the fuel cell under test. The goal is to find a specific frequency or a threshold frequency, at which the RF power enhances the operation of the fuel cell the most. The measurement setups are presented and the polarization curves (Sec. 2.4) are drawn in order to compare the output power between the original fuel cell and the enhanced fuel cell (radio signal applied).

During the work, several fuel cells were constructed in order to measure the output power with and without the influence of the electromagnetic field, fed via the matching part. However, there were severe problems in the first three manufactured fuel cells, and proper measurements could not be conducted. Problems arose from it being impossible to fill the fuel cell entirely, short-circuits and a too low OCV. Also the last fuel cell, with which the final measurements were conducted, faced slight problems, and the operation of the fuel cell was not ideal.

6.1 Measurement Setups

The fuel cell and the matching part were connected according to Fig. 6.1. In a) it is illustrated how the inner conductor is connected, and b) shows the entire matching part connection. The inner conductor has an M10 screw thread, which is screwed around the M10 screw at the end of the fuel cell. The outer conductor of the matching part is placed around the inner conductor, and attached to an SMA-N type coaxial adapter, which in turn is connected to a bias tee. Also the inner conductor of the matching part is connected to the connector, which assures that the inner and outer conductor share the same axis. The bias tee separates the DC voltage from the RF power, which allows feeding high-frequency power through the coaxial input and simultaneously discharging

the fuel cell [54]. An equivalent circuit of a bias tee is presented in Fig. 6.2.

a)

b)
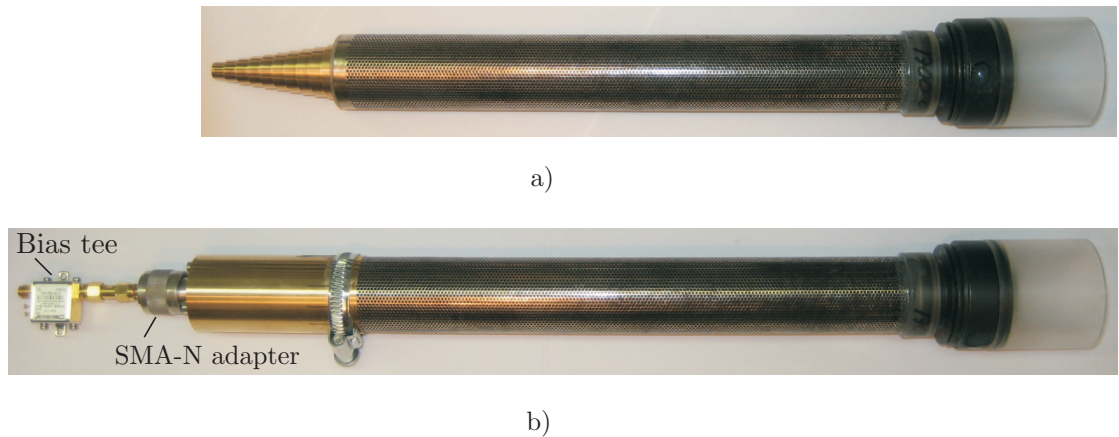
Fig. 6.1: Fuel cell with a) inner conductor of the matching part connected and b) the entire matching part with the bias tee connected.
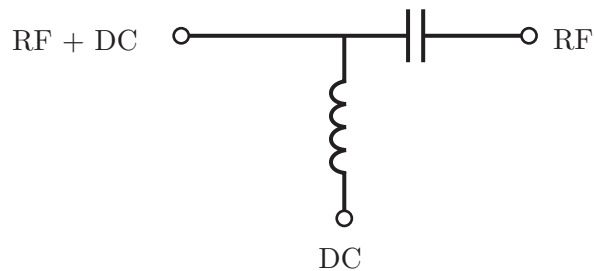
Fig. 6.2: Equivalent circuit of a bias tee [54].

The measurement connections for the power measurements are presented in Fig. 6.3. The fuel cell voltage and the current of the circuit are measured with various resistance levels in order to acquire the polarization curve. The fuel is circulated from the top with a KNF NF30-KTDC mini diaphragm pump in order to enhance the operation. The electromagnetic field is fed from the signal generator through an SMA coaxial cable to the bias tee.

6.1.1 Apparatus

An HP 34970A data acquisition unit is used to measure the voltage and current of the fuel cell. The potentiometer in Fig 6.3 is a General Radio Co. type 102-F variable resistor, which ranges from 0.1 to 111 Ω and has a 0.1 Ω accuracy.

The bias tee ZX85-12G-S+, manufactured by Mini-Circuits, is very broadband (0.2 to 12000 MHz) and offers a low insertion loss (maximally 1.5 dB up to 6 GHz) according to the manufacturer [55]. Measurements show that the insertion loss is approximately 1 dB between 0.1 and 5 GHz.
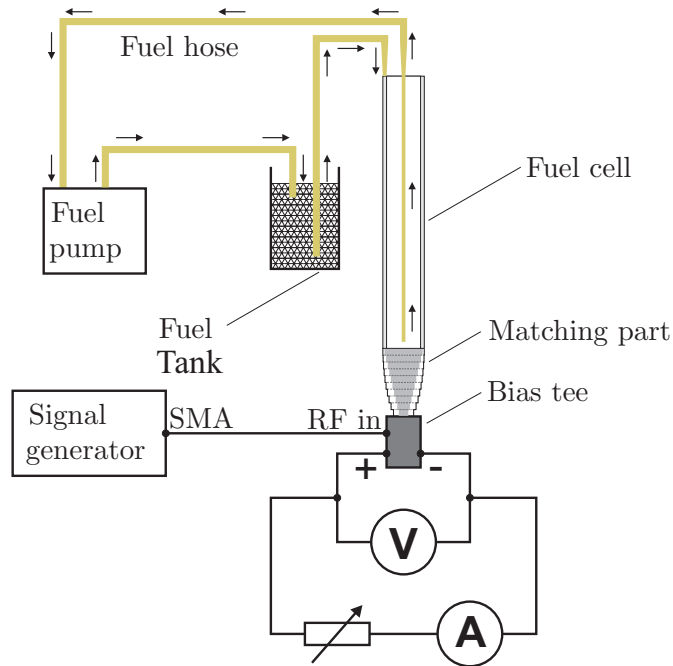
Fig. 6.3: Power measurement setup. The direction of the fuel circulation can be turned.

An HP 8340B synthesized sweeper is used to produce the high-frequency time-harmonic signals. The frequency ranges from 10 MHz to 26.5 GHz with a frequency resolution of 4 Hz and the calibrated output range of the sweeper ranges from -110 to 10 dBm, but can produce powers up to 20 dBm [56]. The device was tested with an Agilent 8564EC spectrum analyzer before conducting the fuel cell measurements. The synthesized sweeper operated without large errors according to the test.

6.2 Measurement Procedure

The measurements were conducted with the measurement setup shown in Fig. 6.3. At first, the fuel solution was fed into the fuel cell, and the fuel was put into circulation with the pump. In the beginning, the potentiometer was not connected, and the OCV was measured. After inserting the fuel, the measured voltage was not immediately stable but the activation of the fuel cell lasted approximately 20 minutes. After the OCV of the fuel cell had stabilized, the potentiometer was connected with a resistance of 111 Ω. In order to get the polarization curve, the resistance was then decreased in steps until a voltage between 0.4 to 0.5 V was obtained. The same procedure was then repeated several times with the signal generator coupled with a frequency of 4 GHz and also without the RF power. The bandwidth of the signal was 100 Hz. The frequency of 4 GHz was chosen due to the fact, that the best results had previously been obtained using this frequency [4]. After each polarization curve measurement, it lasted approximately 20 minutes before

the fuel cell reached a stable OCV. The temperature during the measurements was 24°C. The pump which was utilized to circulate the fuel was found to be necessary in order to keep the fuel cell operating evenly.

The influence of the electromagnetic field was also tested by sweeping the frequency range from 50 MHz to 5 GHz with frequency steps of 100 MHz and comparing the output power. The sweep was completed twice with different voltage levels. The output power of the synthesized sweeper was +15 dBm through all of the measurements. The high power was chosen since it was believed that a higher power would more likely affect the operation of the fuel cell.

6.3 Measurement Results

The measurements of the polarization curves are presented in Table 6.1, where also the resistance levels are visible. The polarization curve was measured 6 times; 3 times without RF energy and 3 times under the influence of a 4 GHz, 15 dBm electromagnetic signal. The power ([mW] column in Table 6.1) was obtained by multiplying the measured voltage and current. The voltage-current and power-current curves are presented in Figs. 6.4 and 6.5.

As can be seen from the measurement results, no evident increase of power can be detected. Even though the polarization curves with the 4 GHz RF signal implemented are slightly better, the enhancement is unsubstantial compared to the variation between the three measurements without RF assistance. From Fig. 6.5 it can be detected, that the fuel cell had not been totally activated and reached its maximal current capacity when the first measurement was performed, since the power-current was not stable until the fourth measurement. The difference between the first three and the last three measurements can be explained by the loosening of one of the fuel hoses, and the shutdown of the fuel circulation that followed. After this incident the OCV increased by approximately 20 mV. It was detected that small changes in the hose position and changing the direction of rotation affected the output voltage and current of the fuel cell more than implementing an EM field.

Instability of the output voltage is caused especially by entrapped air inside the fuel cell. The shape of the measured polarization curves differs from the characteristic polarization curve presented in Sec 2.4. The voltage drop at low currents, which is caused by activation losses, is not visible since the anode catalyst is not functioning properly. Moreover, the maximum power value was not found because the voltage could not be decreased enough without damaging the fuel cell.

Between the second and third measurement (see Table 6.1), the frequency was swept

Fig. 6.4: Measured fuel cell voltage-current curves. The blue lines represent measurements without RF signal and the red dashed lines represent measurements when a 4 GHz EM signal is fed to the fuel cell.

while keeping the fuel cell circuit open (disconnecting the potentiometer). The open circuit voltage was 727 mV before coupling the synthesized sweeper. Then the EM field was coupled and the frequency was changed from 5 GHz to 50 MHz in 100 MHz steps with a time interval of approximately 5 seconds. The voltage remained steadily at 727 mV and did not change. This frequency sweep was repeated with a closed circuit and an output voltage of 605 mV and current of 20.4 mA. Here, the output voltage decreased only because energy was consumed during the test. However, no effect of the electromagnetic field was noticed.

6.3.1 Summary of the Measurements

Before the measurements were conducted it was reasoned that many factors could boost the fuel cell efficiency when an electromagnetic field is applied into the fuel cell. It was assumed, that a high-frequency field would turn the polar molecules in the fuel and potentially break the molecules. It was also pondered, whether the glucose solution could possess a certain oscillation frequency at which this breakdown could occur. In other words, what was the relationship between the photon energy ($E = hf$, where h is
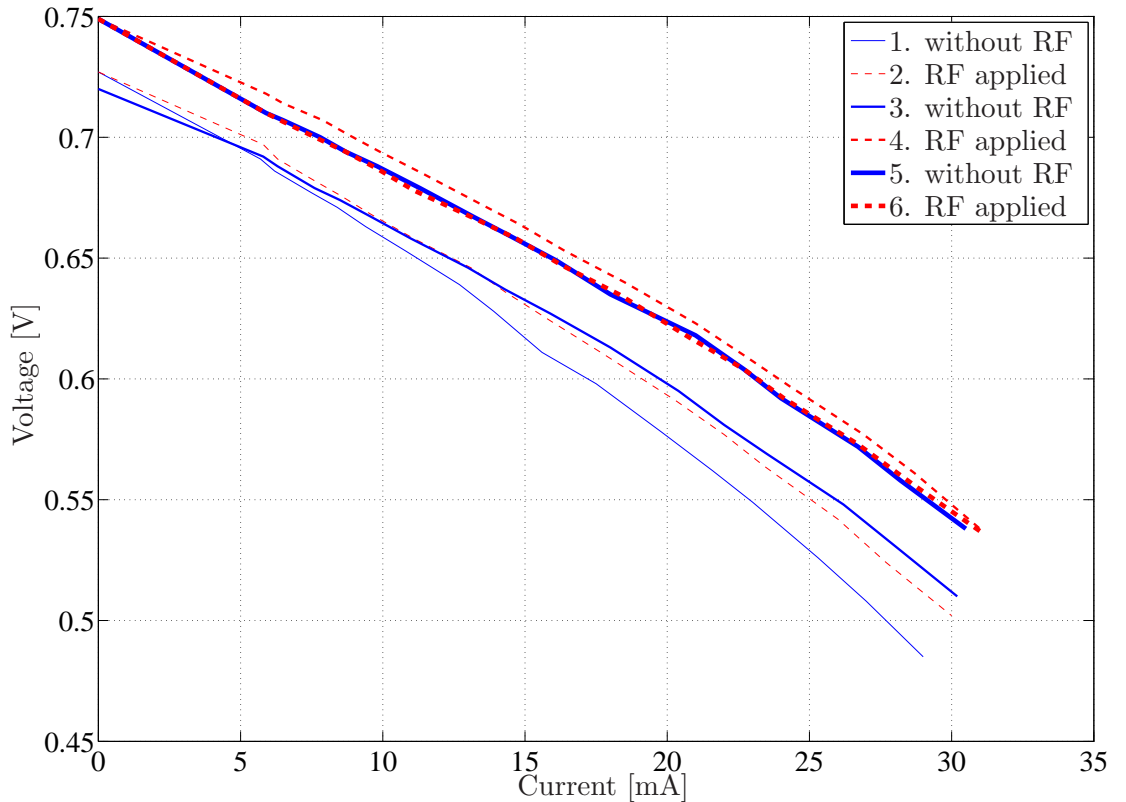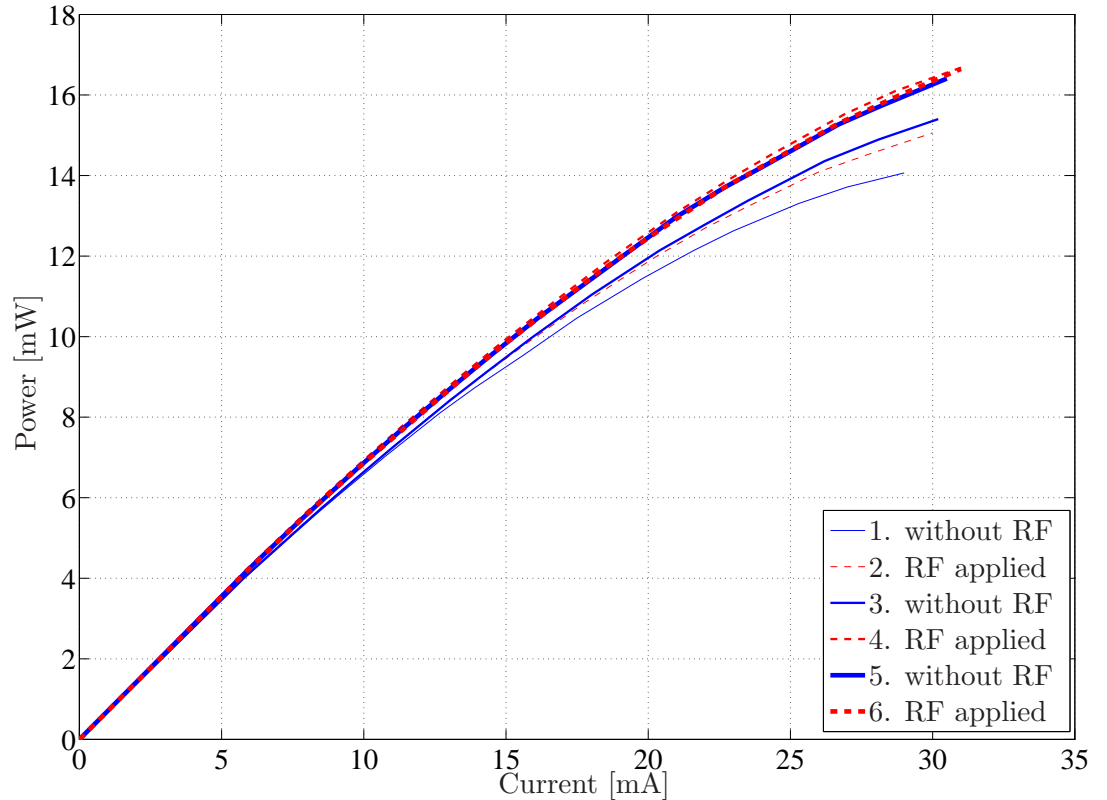
Fig. 6.5: Measured fuel cell power-current curves. The blue lines represent measurements without RF signal and the red dashed lines represent measurements when a 4 GHz EM signal is fed to the fuel cell.

the Planck constant [21]) and the molecular binding energy [57]. The heating effect of an electromagnetic field, that is to say the kinetic heat energy, was also considered [57]. However, these considerations were soon found to be unrealistic since the levels of the photon and kinetic energy were very small.

Yet, the measurements showed no influence of the electromagnetic field on the operation of the fuel cell. Even though the measurements were performed thoroughly, the fuel cell did not operate perfectly at any stage, which throws doubt on the measurement results. The malfunctioning of the fuel cells during this work was a consequence of the fact that the fuel cell itself was a prototype, whose operation was still very much in a development phase. The high attenuation inside the fuel cell results in the electromagnetic field affecting only a small part of the fuel cell when using frequencies over 1 GHz.

6.4 Discussion

In the beginning of the work, positive results that had been obtained in earlier research were examined with great interest, but no measurements were repeated. This could have

been the first step, because the entire work rested on the results of earlier research and assumptions that had been made according to them.

Additionally, the fuel cell prototypes, which were used to test the matching part and whose operation also was measured, did not consist of exactly the same fuel, electrolyte and catalysts as the fuel cell with which earlier research had been performed. Because the fuel cell itself was still developing, the materials and the structure of the fuel cell were modified throughout the work. It would have been reasonable to investigate the effect of the electromagnetic field with a fully functional, perhaps even commercially available fuel cell. Here, problems would have been caused by the difficulties to modify the structure to be suitable for the matching part, but the problems with the basic operation of the fuel cell would have ceased to exist.

The most important part of the work, design of the signal feed into the fuel cell, was done hastily. Here, the structure of the matching part was chosen early almost without considering other possible alternatives. Although the matching part according to simulation results turned out to satisfy the objectives, other feed structures could have been studied more closely.

As has been discussed earlier, a proper circulation of the fuel would benefit the operation of the fuel cell. Although a circulation construction was built, the circulation was not ideal because only one end of the fuel cell was available. This resulted in a situation, where the circulation was very small in some areas. In order to be able to use both ends of the fuel cell for circulating the fuel, another kind of feed structure would be necessary.

Table 6.1: Performed polarization curve measurements.

Ω	1. measurement no EM field [mV]	[mA]	[mW]	2. measurement 4 GHz EM field [mV]	[mA]	[mW]	3. measurement no EM field [mV]	[mA]	[mW]
∞	727	0.0	0.0	727	0.0	0.0	720	0.0	0.0
111	691	5.7	3.9	697	5.8	4.0	692	5.8	4.0
100	686	6.2	4.3	691	6.3	4.4	688	6.3	4.3
80	677	7.5	5.1	682	7.6	5.2	679	7.6	5.2
70	671	8.4	5.6	676	8.5	5.7	674	8.5	5.7
60	663	9.4	6.2	668	9.6	6.4	667	9.6	6.4
50	653	10.8	7.1	658	11.1	7.3	658	11.0	7.2
40	639	12.7	8.1	646	13.1	8.5	646	13.0	8.4
35	628	13.9	8.7	636	14.3	9.1	637	14.3	9.1
30	611	15.6	9.5	624	15.9	9.9	627	15.9	10.0
25	598	17.5	10.5	610	17.8	10.9	613	18.0	11.0
20	578	19.8	11.4	591	20.3	12.0	595	20.4	12.1
17	562	21.6	12.1	577	22.0	12.7	581	22.0	12.8
15	549	23.0	12.6	564	23.4	13.2	569	23.5	13.4
12	526	25.3	13.3	542	26.0	14.1	548	26.2	14.4
10	508	27.0	13.7	524	27.7	14.5	530	28.1	14.9
8	485	29.0	14.1	502	30.0	15.1	510	30.2	15.4

Ω	4. measurement 4 GHz EM field [mV]	[mA]	[mW]	5. measurement no EM field [mV]	[mA]	[mW]	6. measurement 4 GHz EM field [mV]	[mA]	[mW]
∞	749	0.0	0.0	749	0.0	0.0	749	0.0	0.0
111	718	5.9	4.2	710	5.9	4.2	710	5.9	4.2
100	714	6.5	4.6	707	6.5	4.6	707	6.4	4.5
80	707	7.9	5.6	700	7.8	5.5	699	7.8	5.5
70	701	8.8	6.2	694	8.7	6.0	694	8.7	6.0
60	694	9.9	6.9	688	9.8	6.7	687	9.8	6.7
50	685	11.4	7.8	679	11.3	7.7	678	11.1	7.5
40	672	13.5	9.1	667	13.2	8.8	666	13.3	8.9
35	664	14.8	9.8	659	14.5	9.6	658	14.7	9.7
30	653	16.4	10.7	649	16.1	10.4	647	16.3	10.5
25	640	18.5	11.8	635	18.0	11.4	635	18.3	11.6
20	623	21.0	13.1	618	21.0	13.0	617	20.8	12.8
17	609	22.8	13.9	604	22.7	13.7	604	22.7	13.7
15	597	24.3	14.5	592	24.0	14.2	592	24.1	14.3
12	577	26.9	15.5	572	26.7	15.3	573	26.7	15.3
10	561	28.7	16.1	558	28.2	15.7	555	28.8	16.0
8	538	31.0	16.7	538	30.5	16.4	537	31.0	16.6

CHAPTER 7

CONCLUSION

The aim of this thesis was to investigate whether the efficiency of a direct-mode bioorganic fuel cell can be enhanced by means of a time-harmonic, high-frequency electromagnetic field, which was suggested by earlier research. The interest towards fuel cells is steadily increasing because the demand for environmentally friendly alternative energy sources is higher than ever. Bioorganic, glucose fueled fuel cells, that would be beneficial in remote districts, are yet unable to reach desirable power densities.

In this thesis, first, the basics of fuel cell theory relevant to this work were briefly presented. This was needed in order to comprehend and measure the operation of the fuel cell under test. It was noted that the current capacity of the fuel cell under test had been measured to be far below its theoretical maximum. Next, coaxial cable theory was discussed, due to the coaxial structure of the fuel cell. The configuration of the fuel cell under test was presented, and its dielectric materials investigated. The permittivities of the fuel solution and the Carbon-Teflon-Catalyst (CTC) layers were measured with a dielectric probe. For the fuel solution it was detected, that the real and the imaginary part of the relative permittivity decrease with a rising temperature. An increase of concentration was found to decrease the real part of the permittivity, but to increase the imaginary part. Increasing the frequency contributed to the descent of the real part and the rise of the imaginary part of the permittivity. The values were found to be congruent with previously obtained results for the relative permittivity of battery water, varying around $75 - j10$. For the CTC layer, the permittivity was found to be very high, and the loss tangent varied between 1 and 10. The effective relative permittivity was calculated analytically and used to model the combined dielectric, consisting of the fuel solution and the CTC, because modeling two very different dielectric layers with the electromagnetic field simulator would have been problematic. The calculus, which was performed although the permittivity and loss tangent of the CTC was very high, yielded an effective relative permittivity of approximately $180 - j40$.

Applying the EM field inside the fuel cell via a matching part was investigated with means of simulation. A first prototype of the matching part, whose shape and length were restricted due to manufacturing constraints, was manufactured as quickly as possible according to the first simulation results. The tapering methods compared at this point were the constant reflection coefficient, the constant impedance change and the constant diameter change. The brass matching part was found to be fairly broadband, but not optimal in the sense of having the best transmission through the matching part. After further simulations, which also took into account the exponential and the Klopfenstein tapers, the Klopfenstein tapering method was found to be the most optimal. It was also detected, that fewer steps in the taper enhanced the transmission coefficient through the taper. In addition, it was found that lengthening the matching part in general also improved the transmission. The matching part was tapered to the end of the fuel cell, which had a characteristic impedance of 8.4 Ω, and not to the operational part of the fuel cell, where the characteristic impedance was approximately 0.6 Ω. Though it was assumed, that the tapering should have been done to the 0.6 Ω impedance, the simulations proved that both approaches were beneficial, but on different frequency ranges. In order to verify the simulation results, two identical matching parts were connected to each other, in which case the matching part could be measured. It was detected, that the reflection coefficient and the gain through the matching part agreed very well with the measured parameters on the frequency range of 50 MHz to 2 GHz.

The attenuation of the fuel cell was studied with simulations and calculus. Due to the high permittivities and loss tangents of the dielectrics, the attenuation was considerably large. At 1 GHz, the attenuation was calculated to be 1.4 dB/cm. This fact led to the assumption, that when using frequencies above 1 GHz, the influence of the EM field could only exist in the very beginning of the fuel cell, and that especially higher frequencies should be avoided in order to keep the attenuation as low as possible (at 2 GHz the attenuation was 4.8 dB/cm). Finally, also alternative methods for the signal feed were presented, especially in order to free the matching part end of the fuel cell and enable the fuel to circulate. These methods included the probe feed and the radiating cable feed.

The output power measurements were conducted in order to investigate the influence of the electromagnetic field. The goal was to find a specific frequency or a frequency threshold for the EM field, under the influence of which the operation of the fuel cell would be enhanced the most. The pump, which was used to circulate the fuel, was found to be essential from the point of view of the fuel cell since the pump enabled a steady operation of the fuel cell. The polarization curve was first measured without assistance of the RF power by measuring the output voltage of the fuel cell and the current of the load circuit while decreasing the resistance in the circuit with a variable resistor. This procedure was then repeated also with a signal generator at 4 GHz. Totally, the

polarization curve was measured three times with and three times without RF power. The open circuit voltage was measured without the electromagnetic field and then also with the EM field applied, sweeping the frequency from 50 MHz to 5 GHz with steps of 100 MHz. The frequency sweep was also performed while discharging the fuel cell.

The main conclusion of this work is that the measurements were unable to show any significant influence of the time-harmonic, high-frequency electromagnetic field on the output power of the fuel cell. The polarization curves differed slightly from each other, but this was a consequence of the fuel cell, which had not fully been activated before starting the measurements. It is however noted, that the fuel cell was malfunctioning during these measurements. Another problem which was encountered during the measurements was the instability of the fuel cell, in which case the measurement results could not be treated as fully reliable. Especially the anode catalyst did not work properly. This could be seen from the shape of the polarization curves, that did not correspond to the characteristic shape of a normal polarization curve. The malfunction of the fuel cell was a result of the ongoing development process of the fuel cell. In this case the correct electrolyte and catalysts are yet to be found. The results of this work should not be used to draw final conclusions because as mentioned earlier, the fuel cell was malfunctioning. However, the measurements do suggest that the specific combination of the fuel, electrolyte and catalysts used in this application is not influenced by a time-harmonic electromagnetic field within the frequency range of 50 MHz to 5 GHz, which results in no enhancement of the fuel cell operation.

Lastly, it can be concluded that it could have been reasonable to repeat the measurements, which had been reported in earlier research, in the beginning of this work. The effect of changing a single characteristic of the fuel cell could not be found out, since too many properties of the fuel cell was changed during the work.

7.1 Future Prospects

For future research in this issue, a perfectly operating fuel cell would be useful. This would remove a significant part of the uncertainty that was faced in this work. It would furthermore be beneficial if the fuel cell was simply constructed without expensive materials, whereupon manufacturing prototype fuel cells and modifying the construction in order to be suitable for applying the electromagnetic field would be more affordable. In order to make progress in the development process, it is essential to go back to the beginning of the research work and try to repeat the measurements which yielded promising results. While searching for the perfect combination of the fuel, electrolyte and catalysts which might be influenced by electromagnetic signals, only small changes are to be made at a time. Then the effect of EM signals can be studied properly.

BIBLIOGRAPHY

[1] J.-P. Spets, et al., "Starch and cellulose as fuel sources for low temperature direct mode fuel cells," *The Open Fuel Cells Journal*, vol. 1, pp. 1 – 3, Sep. 2008.

[2] ——, "Enhancement of glucose electro-oxidation by an external electromagnetic field in direct-mode fuel cells," *Journal of Power Sources*, vol. 195, no. 2, pp. 475 – 479, Jul. 2010.

[3] J.-P. Spets, M. J. Lampinen, Y. Kiros, T. Anttila, J. Rantanen, and T. Granström, "The simultaneous uses of the direct-mode bioorganic fuel cell and the function generator for the enhancement of the glucose electro-chemical oxidation," *International Journal of Electrochemical Science*, vol. 5, pp. 547 – 555, Apr. 2010.

[4] J.-P. Spets, et al., "The progress in the ongoing development work: Enhancement of glucose electro-oxidation in direct-mode fuel cells - an update," *The Open Fuel Cells Journal*, vol. 2.

[5] C. J. Cleveland, Ed., *Encyclopedia of Energy, Volumes 1 - 6.* San Diego, CA: Elsevier, 2004.

[6] J. Larminie and A. Dicks, *Fuel Cell Systems Explained*, 2nd ed. Chichester, Great Britain: Wiley, 2003.

[7] EG&G Services, Parsons, Inc., and Science Applications International Corporation, *Fuel Cell Handbook*, 5th ed., Morgantown, VA: U.S. Department of Energy, Office of Fossil Energy, National Energy Technology Laboratory, 2000.

[8] C. Rayment and S. Sherwin, "Introduction to fuel cell technology," Univ. of Notre Dame, Dept. of Aerospace and Mech. Eng., Notre Dame, IN, USA, May 2003.

[9] S. Kerzenmacher, J. Ducrée, R. Zengerle, and F. von Stetten, "Energy harvesting by implantable abiotically catalyzed glucose fuel cells," *Journal of Power Sources*, vol. 182, no. 1, pp. 1 – 17, Mar. 2008.

[10] B. Cook, "Introduction to fuel cells and hydrogen technology," *Engineering Science and Education Journal*, vol. 11, no. 6, pp. 205 – 216, Dec. 2002.

[11] Platinum Today, "Current and historical prices," [Online]. Available: www.platinum.matthey.com/cgi-bin/dynamic.pl?template=historical (cited Mar. 25, 2011).

[12] M. Noponen, "Polymeeripolttokennon membraanit," rep. for the course 'Tfy-56.181 A Graduate seminar on Nuclear Energy Engineering', TKK, Espoo, Finland, 2002.

[13] A. Verma and S. Basu, "Direct use of alcohols and sodium borohydride as fuel in an alkaline fuel cell," *Journal of Power Sources*, vol. 145, no. 2, pp. 282 – 285, May 2005.

[14] J.-P. Spets, et al., "Production of glucose by starch and cellulose acid hydrolysis and its use as a fuel in low-temperature direct-mode fuel cells," *Materials Science Forum*, vol. 638–642, pp. 1164 – 1169, Aug. 2009.

[15] M. Kutz, Ed., *Environmentally Conscious Alternative Energy Production.* Hoboken, NJ: Wiley, 2008.

[16] M. Chen, "A compact electrical model for microscale fuel cells capable of predicting runtime and *I-V* polarization performance," *IEEE Transactions on Energy Conversion*, vol. 23, no. 3, pp. 842 – 850, Sep. 2008.

[17] J.-P. Spets, Y. Kiros, M. Kuosa, J. Rantanen, M. Lampinen, and K. Saari, "Bioorganic materials as a fuel source for low-temperature direct-mode fuel cells," *Electrochimica Acta*, vol. 55, no. 26, pp. 7706 – 7709, Nov. 2010.

[18] B. E. Logan, Ed., *Microbial fuel cells.*

[19] J. C. Maxwell, "A dynamic theory of the electromagnetic field," *Royal Society Transactions*, no. 155, pp. 459 – 512, 1865.

[20] D. M. Pozar, *Microwave Engineering*, 2nd ed. New York: Wiley, 1998.

[21] A. Räisänen and A. Lehto, *Radiotekniikan perusteet (Fundamentals in Radio Engineering, in Finnish)*, 12th ed. Helsinki: Otatieto, 2003.

[22] K. Chang, Ed., *Encyclopedia of RF and Microwave Engineering, Volumes 1 - 6.* Hoboken, NJ: Wiley, 2005.

[23] J. R. Apen, "Coaxial cable," in *Mcgraw-Hill encyclopedia of science and technology.* 5th ed., Vol. 3. New York: Mcgraw-Hill, 1982.

[24] R. Mahadevan, "A front-end circuit for full-duplex transmission over coaxial cable," MASc thesis, Dept. Elec. Comp. Eng., Univ. Toronto, Toronto, ON, Canada, 1999.

[25] J. Daintith and E. Martin, Eds., *Dictionary of Science*, 6th ed. New York: Oxford University Press, 2010.

[26] L. Halme, *Johtotransmissio ja sähkömagneettinen suojaus. Osa A (Wire transmission and electromagnetic shielding. Part A, in Finnish)*, 2nd ed. Helsinki: Otakustantamo, 1979.

[27] M. Aoyagi, et al., "Direct high frequency measurement method for small diameter coaxial cable," in *Electronics Packaging Technology, 2003 5th Conference (EPTC 2003)*, Singapore, 10-12 Dec. 2003.

[28] C. R. Paul, *Analysis of Multiconductor Transmission Lines*. Hoboken, NJ: Wiley, 1994.

[29] Microwaves101, "Multi-dielectric coax," [Online]. Available: www.microwaves101.com/encyclopedia/coaxdual.cfm (cited Aug. 11, 2010).

[30] I. Lindell, *Aaltojohtoteoria (Waveguide theory, in Finnish)*. Helsinki: Otatieto, 1997.

[31] R. C. Dorf and J. A. Svoboda, *Introduction to Electric Circuits*, 8th ed. Hoboken, NJ: Wiley, 2010.

[32] M. Philip and W. Bolton, *Technology of Engineering Materials*. Oxford, UK: Elsevier, 2002.

[33] E. Nyfors and P. Vainikainen, *Industrial Microwave Sensors*. Norwood, MA: Artech House, 1989.

[34] W. Wu and C. Smith, "Dielectric measurements using the HP 85070A probe," in *SoutheastCon '92, Proceedings of the IEEE*, Birmingham, AL, 12-15 Apr. 1992, pp. 83 – 86.

[35] *HP 85070A Dielectric Probe Kit (User's manual)*, Hewlett Packard, Santa Rosa, CA, 1990.

[36] J.-P. Spets, private communication, Aug. 2010.

[37] *Fluke 51 & 52 Series II (Users manual)*, Fluke Corp., Everett, WA, 1999.

[38] L. Jylhä, R. Sharma, and A. Sihvola, "Broadband electromagnetic absorption and scattering characteristics of water droplets," Otaniemi, Teknillinen korkeakoulu, Sähkömagnetiikan laboratorio, Tech. Rep., 2000.

[39] A. R. Von Hippel, Ed., *Dielectric Materials and Applications*. Cambridge, MA: MIT Press, 1954.

[40] H. Saito, Y. Suzuki, and M. Taki, "Measurement of complex permittivity for biological cells at 1.7-2.6 GHz by waveguide penetration method," in *URSI 14th General Assembly, K01-2*, Chicago, IL, 7-16 Aug. 2008.

[41] M. Kouzai, A. Nishikata, K. Fukunaga, and S. Miyaoka, "Complex permittivity measurement at millimetre-wave frequencies during the fermentation process of japanese sake," *Journal of Physics D: Applied Physics*, vol. 40, no. 1, pp. 54 – 60, Dec. 2006.

[42] H. Levine and L. Slade, Eds., *Water Relationships in Foods: advances in the 1980s and trends for the 1990s*. New York: Plenum Press, 1991.

[43] C. Bowick, J. Blyler, and C. Ajluni, *RF Circuit Design*, 2nd ed. Burlington, MA: Elsevier, 2007.

[44] B. Riddle, J. Baker-Jarvis, and J. Krupka, "Complex permittivity measurements of common plastics over variable temperatures," *IEEE Transactions on Microwave Theory and Techniques*, vol. 51, no. 3, pp. 727 – 733, Mar. 2003.

[45] VINK, "Tekniset tiedot - PSU (technical data, in finnish)," [Online]. Available: www.vink.com/tuotteet/Tuoteluettelo/PSU—polysulfoni/Tekniset-tiedot—PSU.aspx (cited Jan. 13, 2011).

[46] BASF, *BASF Plastics - key to your success, Ultrason E, Ultrason S*, [Brochure]. Ludwigshafen, Germany, 2007.

[47] R. I. Sarbacher, *Encyclopedic dictionary of electronics and nuclear engineering*. Englewood Cliffs, NJ: Prentice-Hall, 1959.

[48] R. Collin, "The optimum tapered transmission line matching section," *Proceedings of the IRE*, vol. 44, no. 4, pp. 539 –548, Apr. 1956.

[49] HFSS, a FEM based 3D full-wave frequency domain electromagnetic field solver, version 11.2.0, ANSYS Inc, PA, USA. [Online]. Available: www.ansoft.com/products/hf/hfss (cited Mar 30, 2011).

[50] A. Sihvola and I. Lindell, *Sähkömagneettinen kenttäteoria 2. Dynaamiset kentät (Electromagnetic field theory 2. Dynamic fields, in Finnish)*. Tampere: Otatieto, 1996.

[51] M. S. Naidu and V. Kamaraju, *High Voltage Engineering*, 2nd ed. New York: McGraw-Hill, 1995.

[52] G. F. Moore, Ed., *Electric Cables Handbook*, 3rd ed. Cornwall, Great Britain: Blackwell, 1997.

[53] S. R. Saunders and A. Aragón-Zavala, *Antennas and Propagation for Wireless Communication Systems*, 2nd ed. Wiltshire, Great Britain: Wiley, 2007.

[54] M. Tiggelman, K. Reimann, and J. Schmitz, "Reducing ac impedance measurement errors caused by the dc voltage dependence of broadband high-voltage bias-tees," in

Microelectronic Test Structures, 2007. ICMTS '07. IEEE International Conference on, Tokyo, Japan, 19-22 Mar. 2007, pp. 200 – 205.

[55] Mini-Circuits, "Model detailed technical information: ZX85-12G-S+," [Online]. Available: www.minicircuits.com/products/bias_tees_main.html (cited Feb. 1, 2011).

[56] Alliance Test, "HP 8340B Synthesized Sweeper 10 MHz - 26.5 GHz," [Online]. Available: www.alliancetesteq.com//node/14577?gclid=CLzmwZ300qcCFUjxzAodw0wp-Q (cited Mar. 16, 2011).

[57] S. Lang and K. Jokela, "Biofysikaaliset vaikutukset," in *Sähkömagneettiset kentät.* H. Nyberg and K. Jokela (ed.) Säteily- ja ydinturvallisuus -sarja, osa 6. Karisto, Hämeenlinna: Karisto, 2006.